The Stability of the Drygalski Ice Tongue

by

Christine Indrigo

A thesis

presented to the University of Waterloo

in fulfillment of the

thesis requirement for the degree of

Master of Science

in

Geography

Waterloo, Ontario, Canada, 2019

Author's Declaration

This thesis consists of material all of which I authored or co-authored: see Statement of Contributions included in the thesis. This is a true copy of the thesis, including any required final revisions, as accepted by my examiners.

I understand that my thesis may be made electronically available to the public

Statement of Contributions

This thesis is presented in the manuscript option. Chapter 2 contains the manuscript “Drygalski Ice Tongue stability influenced by rift formation and ice morphology” which has been submitted to the *Journal of Glaciology*. Christine Indrigo conducted all analysis and modelling and wrote the manuscript. Christine Dow provided guidance and editorial comments. Jamin Greenbaum provided the ice penetrating radar data. Mathieu Morlighem provided the BedMachine topography data and the ISSM basal velocity and basal melt data.

Abstract

Antarctica has the potential to contribute to sea-level rise by up to 58 m if it were to entirely melt. The Antarctic Ice Sheet is fringed by floating ice in the form of ice shelves and ice tongues, which help to buttress and slow the flow of grounded ice into the ocean. Monitoring the stability of these ice shelves and ice tongues is increasingly important in a warming world, as several areas of floating ice across Antarctica are already experiencing considerable mass loss and thinning due to warming air and ocean conditions. The primary goal of this thesis is to examine several factors contributing to the stability of the Drygalski Ice Tongue in East Antarctica using a combination of remote sensing imagery analysis and subglacial hydrology modelling. The Drygalski Ice Tongue is ~140 km long with an unconfined length of 90 km extending into the Ross Sea. This unconfined length influences local ocean conditions and has a significant control on the size of the nearby Terra Nova Bay polynya, keeping the area free of sea ice. The ice tongue has experienced three large scale calving events in its recorded history since the early 1900s. In this study, Landsat imagery from 1988 to 2018 is used to track the advance of the ice tongue, marginal fracture propagation, and to derive velocity using manual feature tracking. The Glacier Drainage Systems (GlaDS) model is applied to the David Glacier catchment, which feeds into the ice tongue, to reveal the locations and discharge from subglacial channels along the grounding line. These channels are compared with basal channels beneath the floating ice tongue that are identified using airborne radar-derived ice thickness and hydrostatically-derived ice thickness, which can reveal channels in basal draft beneath the ice tongue. The results of this study propose a cyclical relationship between the occurrence of large calving events and large marginal fracture formation, in which large calving events result in the formation of new large fractures where the ice tongue emerges from the coast. When these fractures advance to the ice front, they create an area of weakness where future large calving events can occur. The model output produces three subglacial channels at the grounding line, which align with three channels identified through ice thickness. The propagation of the marginal fractures into the width of the ice tongue is controlled by the presence of these basal channels, as fractures can propagate through the areas of thinner ice in the centre of the northmost channel and stops once they reach the channel keel where ice is thicker. These findings provide insight on the roles that subglacial hydrology, ice draft, and marginal rifting have on ice tongue stability for the Drygalski Ice Tongue and for other floating ice bodies.

Acknowledgements

First, I would like to thank my advisor Dr. Christine Dow for the opportunity not only to work on this thesis, but also to experience glaciology fieldwork and to present my work at an international conference. This thesis wouldn't have been possible without your endless support and guidance.

I would like to thank my parents Sue and Dan for their support throughout my time as a master's student and my entire educational journey.

Thank you to everyone in the cryosphere group for all their feedback and encouragement. Thank you to Margot for your optimism and for listening to all my endless rants. Finally, a big thank you for Jay and Dar for being two of my biggest supporters and for always having confidence in me.

List of Figures

List of Tables

Chapter 1
Introduction

Antarctica is the largest mass of ice on Earth, containing 27 million km^3 of ice (Fretwell et al., 2013). Loss of Antarctica's ice is of increasing concern due to climate change, with the potential to increase global sea level by 58 m if the entire ice sheet were to melt (Fretwell et al., 2013).

Figure 1.1 Map of Antarctica. The Transantarctic Mountains are shown in brown, dividing East and West Antarctica. Ice shelves are shown in light blue, with the study area, the Drygalski Ice Tongue, in the red outline. Map source: Quantarctica Database.

Ice mass in Antarctica is primarily lost due to calving, and basal melting of floating and grounded ice (Rignot & Thomas, 2002), with further losses from sublimation and meltwater runoff at the surface (Shepherd et al., 2012). Calving occurs when ice detaches from the margins

of ice shelves, ice tongues, and tidewater glaciers to form icebergs which are discharged into the ocean. Ice shelves and ice tongues are extensions of glaciers, floating on the ocean while remaining in contact with the grounded ice (Fig. 1.2). Ice tongues are similar to ice shelves; both glacial features drain ice sheets through outlet glaciers and advance past the grounding line, which is the area where grounded ice is no longer in contact with the bed and begins to float on the ocean. However, ice tongues are long and narrow extensions of a glacier, while ice shelves typically fill a basin and are surrounded by grounded ice or land and have a shorter extension into the ocean. Since ice shelves and ice tongues are in direct contact with the ocean, they are sensitive to changes in ocean temperature, where increased temperatures can lead to greater basal melting and ice thinning (Pritchard et al., 2012; Rignot et al., 2013). Basal melting along the ice draft (or underside) of floating ice shelves and ice tongues occurs due to interactions with warm ocean water (Depoorter et al., 2013) or highly turbulent ocean water (Gwyther et al., 2015). Basal melting beneath grounded ice occurs due to geothermal heating, basal friction, and the lower melting point that occurs due to the pressure of the overlaying ice (Dowdeswell & Siegert, 2003; Röthlisberger, 1972; Wright & Siegert, 2012). Sublimation results in the loss of surface snow which converts directly to water vapor without transitioning to liquid water in between, and occurs mostly in the summer months due to the higher amounts of insolation and warmer air temperatures (Van Den Broeke, 1997). Increasing air temperatures can also produce greater amounts of surface meltwater (Doake & Vaughan, 1991). In Antarctica most surface meltwater refreezes, so runoff is a minor component of mass loss (Lenaerts et al., 2012) however, meltwater ponding can lead to the disintegration of ice shelves (Scambos et al., 2000).

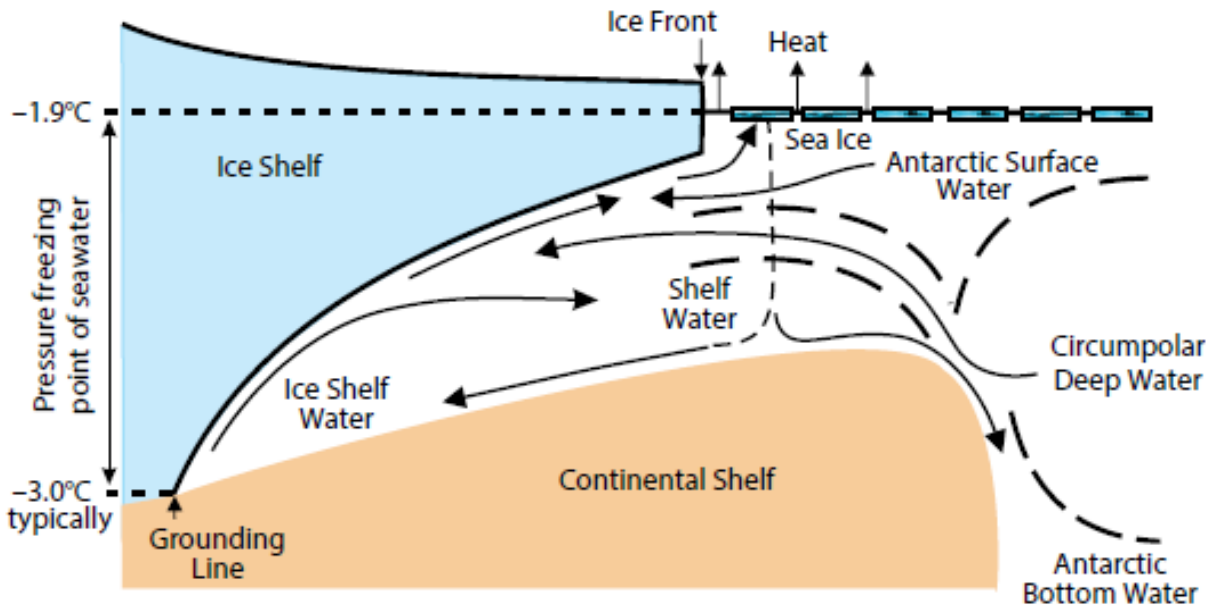

Figure 1.2. Schematic of an Antarctic ice shelf and ocean circulation occurring beneath the ice shelf (Dinniman et al., 2016).

Calving and melting of ice shelves and ice tongues has an indirect impact on sea level rise. As they are already floating in the ocean and are in hydrostatic balance, melting of ice shelves and ice tongues will not lead to an increase in sea level; the volume of water has already been displaced upon flowing past the grounding line and entering the ocean. However, these features act as a buttress to the inland ice due to friction from contact with the land or pinning points (Favier et al., 2012) or from sea ice (Greene et al., 2018; Miles et al., 2017), reducing the flow of ice into the ocean. Loss of the floating ice indirectly influences sea level rise by reducing the buttressing force on outlet glaciers, allowing acceleration of these glaciers and leading to increased ice flow into the ocean, and thus greater mass loss from the Antarctic Ice Sheet (Dupont & Alley, 2005; Fürst et al., 2016).

With increasing global air and ocean temperatures due to climate change, it is important to monitor changes in ice shelf and tongue extent and stability, and to understand the factors contributing to this stability. This is crucial for predicting potential major calving events, which in extreme cases can lead to ice-shelf collapse, as seen with several ice shelves located in the Antarctic Peninsula (Rignot et al., 2004; Rott et al., 2002). Changes in the stability of an ice shelf or ice tongue may indicate shifting ocean conditions such as warmer temperatures, leading to melting of Antarctica's ice shelves and ice tongues (Williams et al., 2002) while also impacting the region's ecology (Meredith & King, 2005). Improving the understanding of the factors

threatening the stability of Antarctica's ice is essential for ice sheet modelling and predicting Antarctica's future in a warming climate. Ice shelf disintegration and rapid retreat due to climate change is already occurring at several areas in the Antarctic Peninsula (Scambos et al., 2000; Scambos et al., 2003; Pritchard et al., 2007) and West Antarctica (MacGregor et al., 2012; Rignot et al., 2014) due to enhanced melting from warming ocean temperatures. In East Antarctica, Wilkes Land has been identified as a large contributor to sea level rise in the past 40 years (Rignot et al., 2019), where Totten Glacier has experienced thinning and may be at risk of future destabilization (Greenbaum et al., 2015).

1.1. Background

1.1.1. Ice shelf and ice tongue stability

Ice shelf and ice tongue stability is influenced by fractures and rift formation, ice-ocean interactions, basal topography of the ocean and grounded ice, and subglacial processes upglacier. Although ice shelves and ice tongues have many similarities, this thesis will focus mainly on ice tongue stability.

Fractures are visual indicators of stress, where stretching or compression of ice results in the formation of cracks in the ice. Surface crevasses originate from the surface of the ice and penetrate downwards, while basal crevasses are situated on the underside and propagate upwards (Colgan et al., 2016). Surface crevasses can become filled with water from surface melting and hydrofracturing can force the crevasse to grow due to the increased pressure on the fracture tip from the presence of denser water, with the potential to propagate through the entire ice thickness (McGrath et al., 2012; Weertman, 1973). When a fracture completely penetrates through the entire thickness of the ice, it is classified as a rift (Benn et al., 2007). Calving events can be classified as either tabular or disintegrating. Tabular calving tends to be infrequent and produces large, flat tabular icebergs that break off from a section of an ice tongue or ice shelf (Liu et al., 2015; van der Veen, 2002). The frequency of calving of large icebergs greater than 500 km^2 is suggested to be between 10-100 years (MacAyeal et al., 2008). Disintegration events can occur rapidly and lead to catastrophic retreat of ice shelves, as seen in the Antarctic Peninsula with the collapse of the Larsen B ice shelf, which disintegrated due to extensive hydrofracturing from ponded surface meltwater (Liu et al., 2015).

Basal topography of the ocean, or bathymetry beneath ice shelves and ice tongues can impact their stability. Pinning points are areas where floating ice becomes grounded on ice rises or ice rumples and can help to stabilize floating ice by providing buttressing and reducing ice flow (Fürst et al., 2016). Ice rises occur where ice flows around the grounded area and ice rumples occur where ice flows over the grounded area (Macayeal et al., 1987; Matsuoka et al., 2015). However, basal topography also has the potential to negatively impact ice shelf and ice tongue stability at the grounding line through marine ice sheet instability (MISI). MISI refers to the positive feedback of retreat that occurs when buttressing is lost and the grounding line retreats on a reverse sloping bed (Mercer, 1978; Schoof, 2007). Most of West Antarctica is classified as a marine ice sheet situated below sea level, along with several sectors along the Antarctic Peninsula and East Antarctica (Frezzotti, 1993; Rignot et al., 2013). These areas are of higher concern and are more sensitive to ice-ocean interactions than areas above sea level, due to their reverse sloping beds where bed elevation increases and ice thickness decreases moving from inland towards the grounding line. As the grounding line retreats to areas of thicker ice, the amount of ice discharged into the ocean increases and previously grounded ice begins to float and thin (Schoof, 2007). Additionally, this retreat can lead to the incursion of circumpolar deep water beneath ice shelves in these marine sectors, leading to ice shelf thinning due to basal melting from the warm water and more grounding line retreat (Favier et al., 2014). Glaciers within the Amundsen Sea Embayment have started to experience MISI-driven ice shelf thinning and grounding line retreat (Favier et al., 2014; Joughin et al., 2014; Rignot et al., 2014).

1.1.2. Subglacial hydrology

Water flows beneath the Antarctic Ice Sheet through subglacial networks in an efficient channelized or inefficient distributed system (Dow et al., 2018b; Le Brocq et al., 2013). Subglacial water flow is driven by the hydraulic potential gradient, where water flows from high to low hydraulic potential (Shreve, 1972). Hydraulic potential ϕ (Pa) is defined by:

$$\phi = P_w + \rho_w g z \quad (1)$$

where P_w is the water pressure (Pa), ρ_w is the density of water (kg m^{-3}), g is the acceleration due to gravity (m^2 s^{-1}), and z is the elevation (m) (Shreve, 1972). Effective pressure N (Pa) is the

difference between the ice overburden pressure, which is the pressure imposed on the channel due to the weight of the ice above, and water pressure defined by

$$N = P_i - P_w \quad (2)$$

where P_i is the ice pressure (Pa) which is

$$P_i = \rho_i g H \quad (3)$$

where ρ_i is the density of ice (kg m^{-3}) and H is the ice thickness (m) (Röthlisberger, 1972). When water is at overburden pressure, the ice surface slope has a greater influence on the direction of flow than the bed slope, allowing for subglacial water to flow uphill, following the surface slope (Shreve, 1972; Siegert et al., 2016).

Channelized systems occur with high volumes of meltwater and are lower pressure systems than the surrounding distributed system (Röthlisberger, 1972). Channels may be incised into the bed as Nye (N-) channels (Nye, 1976) or incised into the ice as Röthlisberger (R-) channels (Röthlisberger, 1972). These channels grown and shrink depending on the water pressure and the ice overburden pressure. Where water pressure is lower than the ice overburden pressure, channels begin to close and where water pressure is greater than the ice overburden pressure, channels grow larger (Röthlisberger, 1972).

Subglacial water beneath grounded ice impacts basal melt rates and also increases the velocity by lubricating the bed and allowing the ice above to flow faster when this water is highly pressurized. This is especially concerning when there is subglacial water flux over the grounding line, as this area is the last point of contact that the ice has with the bedrock. This water can form basal channels under ice shelves due to the discharge of buoyant freshwater from the subglacial channels entraining warmer ocean water (Le Brocq et al., 2013; Alley et al., 2016). As the subglacial hydrology of the Antarctic Ice Sheet is challenging to directly observe, methods such as satellite altimetry, seismic sounding, ice penetrating radar, and numerical modelling are used to infer the locations of subglacial lakes (Wright & Siegert, 2012) and channels (Schroeder et al., 2013; Dow et al., 2020)..

The stability of ice shelves and ice tongues in Antarctica is influenced by several controlling factors. MISI threatens to destabilize several areas in West Antarctica with rapid

grounding line retreat and thinning; fractures and rifting can lead to mass loss through calving; and subglacial channels beneath grounded ice and melted through ice-ocean interaction can influence the ice draft morphology beneath floating ice. The overall purpose of this study is to investigate the factors contributing to the stability of the Drygalski Ice Tongue, a large ice tongue in East Antarctica that extends unconfined for ~90 km into the ocean. To achieve this, the evolution of the advance of ice tongue, the propagation of large fractures, and the role of subglacial hydrology in the stability of the Drygalski Ice Tongue will be examined.

1.2. Research Objectives

The Drygalski Ice Tongue is relatively understudied in comparison to ice tongues in Greenland and considerably less than the large ice shelves across Antarctica, likely due to its relatively stable history. Despite this, studying the Drygalski Ice Tongue and its source, David Glacier is important for improving the understanding of ice tongues, their buttressing effect, and their stability. Additionally, understanding the calving processes of the Drygalski Ice Tongue is important for ship access to the research stations in the nearby Terra Nova Bay area. This access is currently possible due to the Terra Nova Bay polynya, which is an area of open ocean that is surrounded by sea ice. Access could be impacted by major calving of the tongue leading to a smaller polynya size and thus allowing for more sea ice to enter Terra Nova Bay from the Ross Sea or to form locally.

The primary research objectives of this research are:

1. To conduct an analysis of changes in velocity, mass loss, and fracture formation of the Drygalski Ice Tongue
2. To simulate subglacial water movement throughout the David Catchment allowing for the identification of channelized water output at the grounding line
3. To examine the relationship between calving events, velocity, fractures, and basal channels and establish how they influence the stability of the Drygalski Ice Tongue

1.3. Thesis Structure

This thesis consists of 3 chapters and follows the manuscript thesis format. Chapter 1 is the introductory chapter to this thesis, providing a background on the study area, a literature

review, overview of the methods, and the objectives of this research. Chapter 2 includes the manuscript submitted to the Journal of Glaciology titled *Drygalski Ice Tongue stability influenced by rift formation and ice morphology*. The final chapter contains conclusions from this research, addresses the initial research objectives, and provides recommendations for future research.

1.4. Study Site

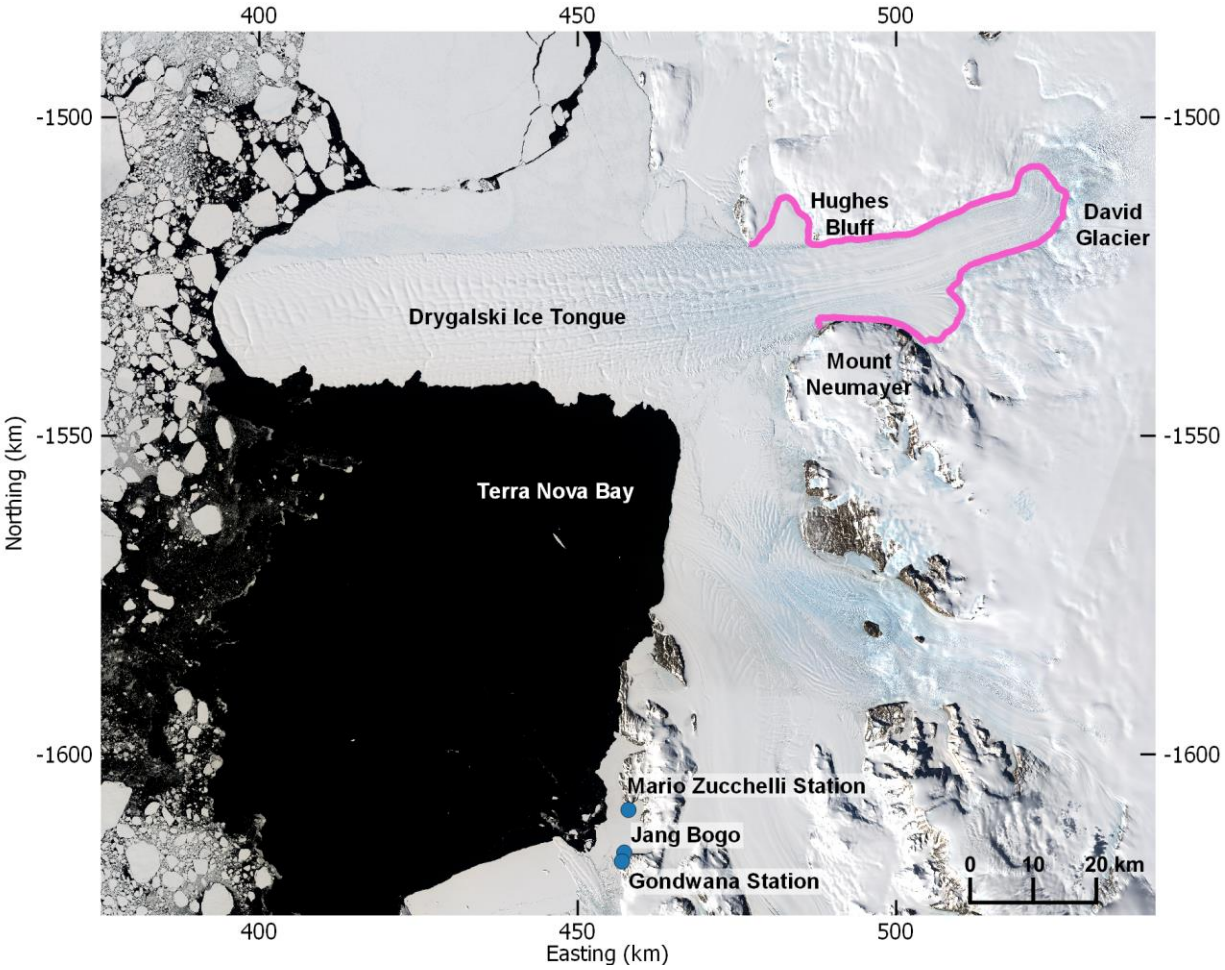

Figure 1.3. Map of the study area of David Glacier and the Drygalski Ice Tongue, with Terra Nova Bay to the north. Study area is in UTM zone 58C. The grounding line is outlined in pink. The location of three nearby research stations (Mario Zucchelli, Gondwana, and Jang Bogo) are indicated by blue circles. Image sources: Landsat 8 OLI/TIRS path 60 row 113, acquisition date: 23 December 2017; Landsat 8 OLI/TIRS path 61 row 114, acquisition date: 30 December 2017; Landsat 8 OLI/TIRS path 62 row 113, acquisition date: 6 January 2018.

1.4.1. David Glacier

David Glacier is situated on the Scott Coast of East Antarctica and flows between Mount Joyce and Mount Priestley within the Prince Albert Range of the Transantarctic Mountains, as visible in Fig. 1.1 and 1.3 (Frezzotti, 1993; Lucchitta et al., 1993). David Glacier is the largest outlet glacier in Victoria Land, East Antarctica (Fea et al., 2013). Outlet glaciers drain interior ice sheets, terminating on land or into the ocean. The David Glacier drains Dome C and Talos Dome of the interior Antarctic Ice Sheet (Lugli & Vittuari, 2017), and covers an area of around 213,500 km^2 (Rignot et al., 2019). The David Cauldron is an icefall where several flows converge and form into the David Glacier as it passes over a subglacial ridge (Frezzotti, 1993; Rignot, 2002) and forms the Drygalski Ice Tongue as it loses contact with the bed. After this icefall, the glacier flows through a deep valley between the two mountains (Rignot, 2002). A large portion of the glacier is situated below sea level, making the David Glacier a marine glacier in addition to an outlet glacier (Frezzotti, 1993). Similar to glaciers in West Antarctica, this position below sea level makes the David Glacier highly sensitive to climate change and is concerning due to its potential contributions to sea level rise. Beneath the David Glacier catchment, several subglacial lakes which actively grow and drain have been identified, suggesting that there is a temporally variable hydrological system (Smith et al., 2009; Wright & Siegert, 2012). The grounding line area of the David Glacier-Drygalski Ice Tongue has been found to have a high basal melt rate (29 ± 6 m by Rignot (2002); 20.91 ± 9.6 m by Wuite et al. (2009)), which decreases moving downstream along the ice tongue. Both findings determined basal melt rate based on accumulation and mass flux over a cross-section at the grounding line (Rignot, 2002; Wuite et al., 2009).

1.4.2. Drygalski Ice Tongue

The Drygalski Ice Tongue is an extension of the David Glacier. In 2018 it was 140 km long from the grounding line to the terminus, with a 90 km section of this extending unconfined into the Ross Sea. In comparison, the nearby Erebus Ice Tongue south of the Drygalski Ice Tongue was only 12 km long in 2009 (Stevens et al., 2014) and Campbell Glacier Tongue to the north of the Drygalski Ice Tongue was only 14.5 km long in 2018. The ice tongue was first visited in 1900 by Carsten Borchgrevink, a polar explorer, but was not identified or named until

it was explored by Robert Falcon Scott, another polar explorer, in 1902 (Frezzotti & Mabin, 1994). In addition to being a geographical anomaly due to the extensive length of the unconfined section in the open ocean, the ice tongue has an effect on its surrounding area. The Drygalski Ice Tongue influences Terra Nova Bay to the north of the ice tongue, by keeping Terra Nova Bay free from drifting sea ice, controlling the size of the Terra Nova Bay polynya depending on the length of the ice tongue (Frezzotti & Mabin, 1994). Polynyas are areas of open water surrounded by sea ice and are considered to be sea ice factories (Frezzotti, 1997). The ice-free open water allows for the formation of sea ice, while strong katabatic winds pushes this ice away and maintains the polynya (Cappelletti et al., 2010). The Terra Nova Bay polynya contributes to the production of high salinity shelf water (HSSW) in the Ross Sea, and it is estimated that this polynya is responsible for generating 5 - 15% of the sea ice over the Ross Sea continental shelf (Frezzotti & Mabin, 1994; Frezzotti, 1997; Kurtz & Bromwich, 1985). HSSW is dense water that is produced as a result of the salt that is released through the formation of sea ice (Holland et al., 2007). HSSW in the Ross Sea contributes to Antarctic Bottom Water (Fusco et al., 2009; Cappelletti et al., 2010), which is an important component of the global thermohaline circulation (Jacobs, 2004).

The Drygalski Ice Tongue is currently the longest ice tongue in Antarctica (Stevens et al., 2017), yet the reasons for its ability to extend so far into the ocean are not fully understood. Both the David Glacier and the Drygalski Ice Tongue are fast moving, especially at the terminus of the ice tongue with velocity speeds upwards of 750 m/yr (Frezzotti & Mabin, 1994; Wuite et al., 2009). The average velocity of the entire David Glacier-Drygalski Ice Tongue is around 700 m/yr (Fountain et al., 2017). The base of the ice tongue has a rippled morphology as identified by Bianchi et al. (2001a), which is reflected on the surface as depressions as an effect of hydrostatic adjustment where the ice is in hydrostatic balance. The ice tongue becomes supported by bedrock closer to the grounding line, where the floating ice will not be in hydrostatic balance. Areas where floating ice is in contact with pinning points will have this same effect.

Five several kilometer-long fractures exist along the north edge of the ice tongue, with both the north and south edges exhibiting jagged edges with hundreds of smaller fractures. Multi-year landfast sea ice (i.e. sea ice that is fastened to land or to another body of ice such as ice shelves and ice tongues) forms along the north edge of the tongue, persisting for up to 35 km

along its length. Landfast sea ice also forms along the south edge but breaks up and does not typically persist. However, between 2000 and 2006 several large icebergs persisted in the Ross Sea, preventing the landfast sea ice from breaking up between the south edge of the ice tongue and Ross Island located ~18 km to the south, and leading to the formation of multi-year landfast sea ice (MacAyeal et al., 2008). The ice tongue loses mass primarily through basal melting and through calving at the terminus, with three known calving events occurring: in the early 1900s (Frezzotti & Mabin, 1994; Holdsworth, 1985), between 1956 to 1957 (Frezzotti & Mabin, 1994), and between 2005 to 2006 (Parmiggiani & Fragiacomo, 2005; Wuite et al., 2009). This recent calving event, referred to in this thesis as the 2005-2006 calving event, consisted of three separate calving events. In February 2005, 74.3 km^2 calved off from the ice front (Parmiggiani & Fragiacomo, 2005). An additional 64.5 km^2 was lost in April 2005 when iceberg B-15 collided with the terminus, leaving a small tip remaining (Wuite et al., 2009). On 29 March 2006 the remaining portion of this tip was broken off when iceberg C-16 collided with the ice tongue, squaring off the ice front shape (MacAyeal et al., 2008).

1.5. Methods

This thesis uses a combination of remote sensing methods and numerical modelling to address the research questions outlined in section 1.3. The remote sensing data consist of satellite imagery and airborne radar data. All satellite imagery used are from multispectral sensors as part of the of U.S. Geological Survey (USGS) Landsat program, which has been continuously operating satellites since 1972 (U.S. Geological Survey, 2016). Multispectral sensors measure solar energy that is reflected from the earth back to the sensor, covering multiple bands of the electromagnetic spectrum including visible, near infrared, and thermal infrared (Tedesco, 2015).

1.5.1. Satellite Imagery

Landsat and other optical sensors require solar illumination limiting data collection to the summer months in Antarctica, and suitable data are further limited by cloud cover which obscures the Earth's surface (Tedesco, 2015). Due to the absence of sunlight during the winter months in Antarctica, Landsat data are only available for months between September to March

for the study area. High percentages of cloud cover throughout a scene or clouds obscuring the terminus of the ice tongue inhibit the use of that scene for analysis.

Landsat scenes were used to measure changes in the shape and length of the ice tongue and the advection of fractures using a manual feature tracking method outlined in section 1.5.6. A single scene was selected per year for the span of available satellite data from 1988 to 2018, in order to track changes on an annual basis. For consistent measurements of the changes in front position and advection of fractures, scenes captured in December were ideal, as these scenes appeared to have the least amount of cloud cover in comparison to other months. Additionally, the Drygalski Ice Tongue is surrounded by less sea ice in December than in September to November, allowing for easier identification of the ice tongue front. For instances where December scenes were unavailable or unsuitable, the closest suitable scenes were selected. As this research uses optical satellite imagery, selecting multiple cloud-free images per year that are suitable for analysis is difficult. In order to increase the data coverage throughout the year, especially over the austral winter, radar imagery would be required.

Table 1. List of Landsat (4-8) scenes used in this study including the acquisition date, sensor, and spatial resolution.

Scene ID	Acquisition Date	Satellite	Sensor	Spatial resolution
LT04_L1GS_060114_19881215_20170205_01_T2_B4	15 December 1988	Landsat 4	TM	30 m
LT04_L1GS_062113_19890303_20170204_01_T2_B1	3 March 1989			
LT04_L1GS_062113_19900117_20170131_01_T2_B3	17 January 1990			
LT04_L1GS_063113_19920215_20170124_01_T2_B1	15 February 1992			
LT05_L1GS_062113_19910128_20170127_01_T2_B3	28 January 1991	Landsat 5	TM	30 m
LE07_L1GT_060114_19991230_20170215_01_T2_B8	30 December 1999	Landsat 7	ETM+	15 m
LE07_L1GT_059114_20000124_20170213_01_T2_B8	24 January 2000			
LE07_L1GT_061113_20010209_20170207_01_T2_B8	9 February 2001			
LE07_L1GT_061113_20011226_20170201_01_T2_B8	26 December 2001			
LE07_L1GT_060114_20020104_20170201_01_T2_B8	4 January 2002			
LE07_L1GT_062113_20021204_20170127_01_T2_B8	4 December 2002			
LE07_L1GT_061113_20030114_20170127_01_T2_B8	14 January 2003			
LE07_L1GT_060114_20050128_20170116_01_T2_B8	28 January 2005			
LE07_L1GT_060114_20061217_20170106_01_T2_B8	17 December 2006			
LE07_L1GT_061114_20071211_20170101_01_T2_B8	11 December 2007			
LE07_L1GT_060114_20081120_20161224_01_T2_B8	20 November 2008			
LE07_L1GT_060114_20081206_20161224_01_T2_B8	6 December 2008			
LE07_L1GT_061114_20091216_20161218_01_T2_B8	16 December 2009			
LE07_L1GT_060114_20101212_20161211_01_T2_B8	12 December 2010			
LE07_L1GT_060114_20111113_20161205_01_T2_B8	13 November 2011			
LE07_L1GT_060114_20111215_20161204_01_T2_B8	15 December 2011			
LE07_L1GT_061114_20121208_20161128_01_T2_B8	8 December 2012			
LC08_L1GT_059114_20131103_20170428_01_T2_B8	3 November 2013	Landsat 8	OLI/ TIRS	15 m
LC08_L1GT_058114_20131214_20170427_01_T2_B8	14 December 2013			
LC08_L1GT_062113_20141229_20170415_01_T2_B8	29 December 2014			
LC08_L1GT_060114_20151218_20170331_01_T2_B8	18 December 2015			
LC08_L1GT_059114_20161127_20170317_01_T2_B8	27 November 2016			

LC08_L1GT_219130_20161214_20170316_01_T2_B8	14 December 2016
LC08_L1GT_062113_20171119_20171205_01_T2_B8	19 November 2017
LC08_L1GT_061114_20171230_20180103_01_T2_B8	30 December 2017
LC08_L1GT_060114_20181124_20181124_01_RT_B8	24 November 2018
LC08_L1GT_061114_20190323_20190403_01_T2_B8	23 March 2019

Landsat products were acquired from the USGS EarthExplorer and LandsatLook Viewer services. Landsat 7 and 8 scenes are Tier 2 (T2) data products with L1GT level processing and older Landsat scenes (Landsat TM 1-5) are T2 with L1GS level processing. These data are Collection 1 products with geometric corrections but have not been co-registered for this research which may introduce error in analysis between scenes. Additionally, minor measurement errors may result from the difference in spatial resolution between older (30 m resolution) and newer (15 m resolution) Landsat products All Landsat data were downloaded in GeoTIFF format and projected in the EPGS:3031 WGS 84/Antarctic Polar Stereographic coordinate reference system with the WGS 84 Ellipsoid.

Landsat 4, launched in 1982, and Landsat 5, launched in 1984, were both equipped with the Multispectral Scanner System (MSS) and Thematic Mapper (TM) instruments (U.S. Geological Survey, 2018). Only imagery using the Thematic Mapper is used in this research. The band used for each scene in feature tracking analysis was selected based on the ability to visually distinguish between ice, water, and sea ice, as spatial resolution of all bands 1-4 are the same (30 m). The band with higher contrast between the ice tongue and surrounding water or sea ice was selected. Each scene along with the band used is listed in Table 2.

Table 2: Bands used for Landsat 4-5 scenes.

Date	Satellite	Band
1988-12-15	Landsat 4 TM	Band 4 – Near Infrared (NIR)
1989-03-03	Landsat 4 TM	Band 1 – Blue
1990-01-17	Landsat 4 TM	Band 3 – Red
1991-01-28	Landsat 5 TM	Band 3 – Red

Landsat 7, launched in 1999, introduced the panchromatic band with a spatial resolution of 15 metres (U.S. Geological Survey, 2018). The panchromatic band is a single band covering a

larger wavelength range and has a higher spatial resolution that the other bands (Tedesco, 2015). This band is selected for all imagery used in this research from the Landsat 7 Enhanced Thematic Mapper Plus (ETM+) sensor. In addition to the benefit of a higher spatial resolution, there is also greater visible contrast between ice and water using the panchromatic band for analysis compared to the other 7 bands. In 2003 the scan line corrector (SLC) of the Landsat 7 ETM+ sensor permanently failed (U.S. Geological Survey, 2018). The SLC was responsible for compensating for the satellite's forward motion as it collected data and the failure of this instrument has resulted in areas of missing data that are visible in the form of black lines throughout some scenes from 2003 onwards (U.S. Geological Survey, 2018). An example of a scene with large areas of missing data is shown below in Fig. 1.4.

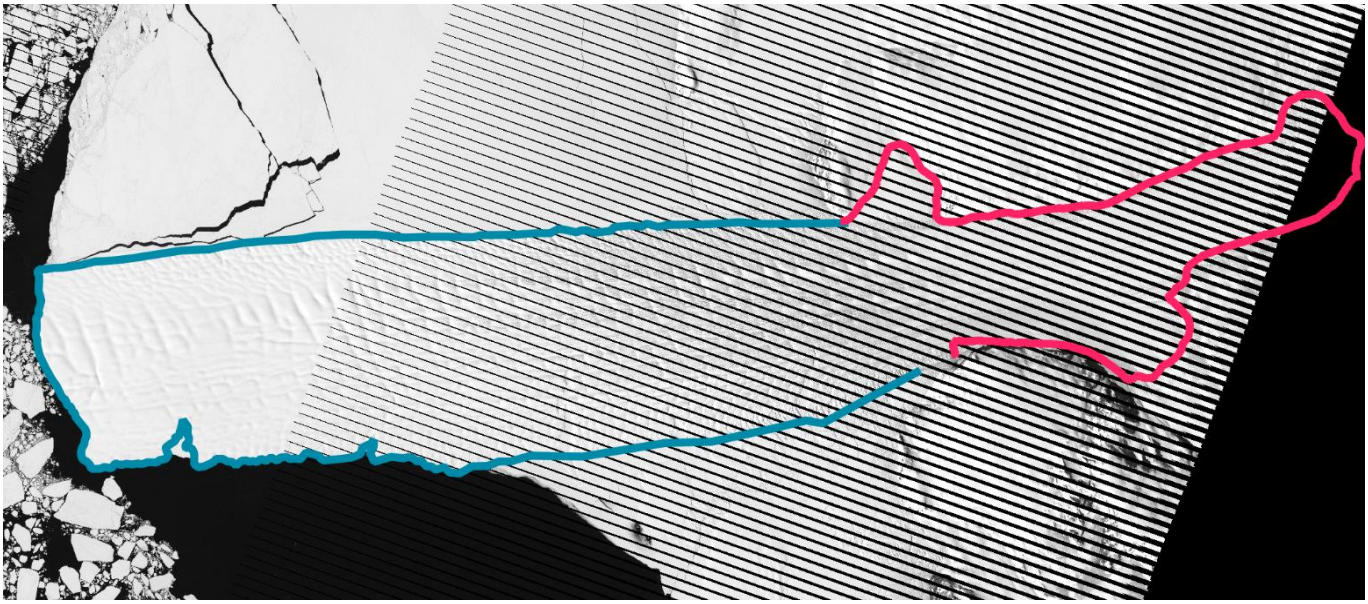

Figure 1.4. Example of Landsat 7 imagery (December 17, 2006) with missing data, visible as the diagonal black lines throughout the scene. Pink line indicates the grounding line. Blue line indicates the outline of the unconfined extent in 2006.

Landsat 8 was launched in 2013 with new sensors, the Operational Land Imager (OLI) and the Thermal Infrared Sensor (TIRS) (U.S. Geological Survey, 2016). Landsat 8 imagery has 11 bands compared to 8 bands with Landsat 7. All Landsat 8 imagery used in this research are in the panchromatic band from the OLI sensor. The panchromatic band has a spatial resolution of 15 m while the other bands have a 30 m resolution (U.S. Geological Survey, 2016).

1.5.2. Ice penetrating radar

Airborne ice penetrating radar data (IPR) were collected by the University of Texas Institute for Geophysics (UTIG) as part of the International Collaborative Exploration of the Cryosphere by Airborne Profiling (ICECAP) project in October 2011. Four transect lines of radar-measured ice thickness running across the width of the ice tongue were used in this study to identify basal channels beneath the ice tongue: DVG/JKB2e/Y05a, DVG/JKB2e/Y10a, DVG/JKB2e/Y14a, and DVG/JKB2e/Y18a (Fig. 1.5). These transects were collected on 28 November 2011 using a custom UTIG-designed IPR system, the High Capability Airborne Radar Sounder (HiCARS) 2 with a centre frequency of 60 MHz, aboard a DC-3T aircraft (Blankenship et al. 2012).

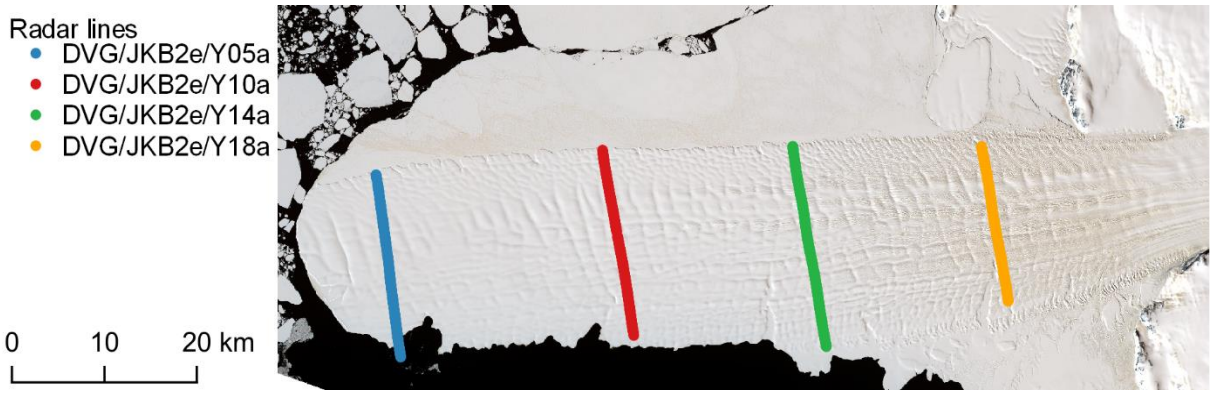

Figure 1.5. UTIG ice penetrating radar transects along the width of the ice tongue. Image source: natural colour (bands 4-3-2) Landsat 8 OLI/TIRS path 61 row 114, acquisition date: 30 December 2017.

1.5.3. Reference Elevation Model of Antarctica

The Reference Elevation Model of Antarctica (REMA) is an 8-metre resolution Digital Elevation Model (DEM) of Antarctica's surface developed by the Polar Geospatial Centre at the University of Minnesota (Howat et al., 2019). For analysis in this thesis, the DEM was interpolated from 8 m resolution to 25 m resolution due to file size limitations. Surface elevations were converted from the WGS84 ellipsoid to the GL04c geoid to be relative to sea level. From this surface DEM, ice thickness (H) was derived based on the following hydrostatic equilibrium equation following Van den Broeke et al. (2008):

$$H = \frac{(Z_s - \Delta h)\rho_w}{\rho_w - \rho_i} + \Delta h;\ \Delta h = h_f(1 - \rho_f/\rho_i) \quad (4)$$

where Z_s is the surface elevation (metres above sea level), Δh is the firn depth correction, h_f is the thickness of the firn layer, ρ_w is the density of seawater (1028 kg m^{-3}), and ρ_i is the density of ice (917 kg m^{-3}). Firn is the stage between snow and glacial ice and has a density between 550 kg m^{-3} and 830 kg m^{-3} (Van den Broeke, 2008). Δh is required to correct for this difference in density between the firn layer and the solid ice beneath it. As the actual firn thickness along the Drygalski Ice Tongue is unknown, Δh was estimated using ice thickness data from the airborne ice penetrating radar lines collected by UTIG. The Δh values were estimated based on the difference between the radar-derived ice thickness and the hydrostatically-derived ice thickness. To do this, values for the hydrostatically-derived ice thickness were extracted along each of the four UTIG transect lines (Y05a, Y10a, Y14a, and Y18a) and Δh values in equation 1 were adjusted to best match the hydrostatic thickness to the radar-derived thickness. The Δh along Y018a is 0 m while the other lines range from values of 12 m to 18 m. These Δh values were then linearly interpolated along the ice tongue to adjust for firn in the ice thickness equation applied to the REMA surface elevation DEM. Basal draft is the thickness of the ice below sea level and is determined by subtracting the ice thickness DEM from REMA's surface DEM. Basal draft is used to identify basal channels running along the bottom of the ice tongue.

1.5.4. BedMachine surface and bed elevation

The BedMachine Antarctica project by the Ice Sheet Modeling Group at the University of California Irvine provides ice thickness and bed topography data for grounded and floating ice. Surface elevations are also included from REMA. Ice thickness data within the David catchment area are primarily derived using a streamline diffusion approach in the slower upstream region, while the area from the grounding line to 260 m upstream is derived using mass conservation. The streamline diffusion approach is an anisotropic method of interpolating ice thickness for areas between radar flight lines (Morlighem et al., 2019). The mass conservation approach to calculating ice thickness combines ice penetrating radar measurements of ice thickness with inversions of ice velocity data to interpolate ice thickness over a larger area (Morlighem et al., 2011). BedMachine surface, bed elevation, and ice thickness data have a grid spacing of 500 m and are used in the GlaDS model described in section 1.5.7. Within the subglacial catchment area

for David Glacier, bed elevations range from -1152 m to 1788 m asl; surface elevations range from 15m to 2758 m asl.

1.5.5. Basal velocity and melt rate

Variable basal velocity and basal melt rates have been modelled with the Ice Sheet System Model (ISSM) using a higher order model for stress balance (Pattyn, 2003; Morlighem, 2011). These data come from the UCIJPL_ISSM modelling as part of the Ice Sheet Model Intercomparison Project for CMIP6 (ISMIP6) (Seroussi et al., 2019). Topography inputs for the ISSM modelling are based on Bedmap2 (Seroussi et al., 2019). These data are inputs used in the GlaDS model described in section 1.5.7 and have a grid spacing of 1 km. Within the subglacial catchment area for David Glacier, basal velocity values range from 0.0474 m a^{-1} to 726 m a^{-1} but are capped at a maximum of 500 m a^{-1} for modelling (Fig. 1.6). Basal melt rates range from 0 m a^{-1} to 0.465 m a^{-1} (Fig 1.6).

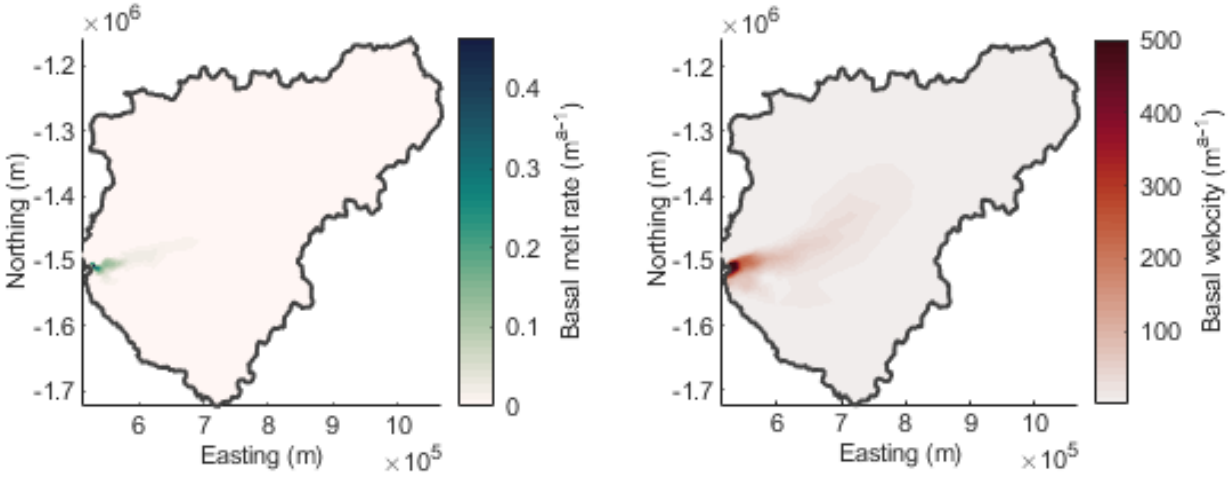

Figure 1.6. Basal melt rate (left) and basal velocity (right) for the David Glacier catchment area.

1.5.6. Velocity measurements

Ice tongue velocity estimates were determined using manual feature tracking of the five large prominent fractures for each year of available imagery between 1988 and 2018. This process involved measuring the displacement of a feature between two scenes in QGIS. The EPSG:3031 WGS 84/Antarctic Polar Stereographic coordinate reference system and the WGS 84 ellipsoid were used in measuring displacement distances for all scenes. To ensure consistency in velocity measurements, three sets of three guide lines following the direction of flow were

created for each rift to cover the entire length of the rifts (Fig. 1.**7** and 1.8). Along these guide lines, the displacement of an individual, distinct pixel was measured between two scenes spaced approximately one year apart. Between 8 to 18 measurements per annual time period were taken along the left and right sides of each rift along each guide line, and averaged to account for measurement errors.

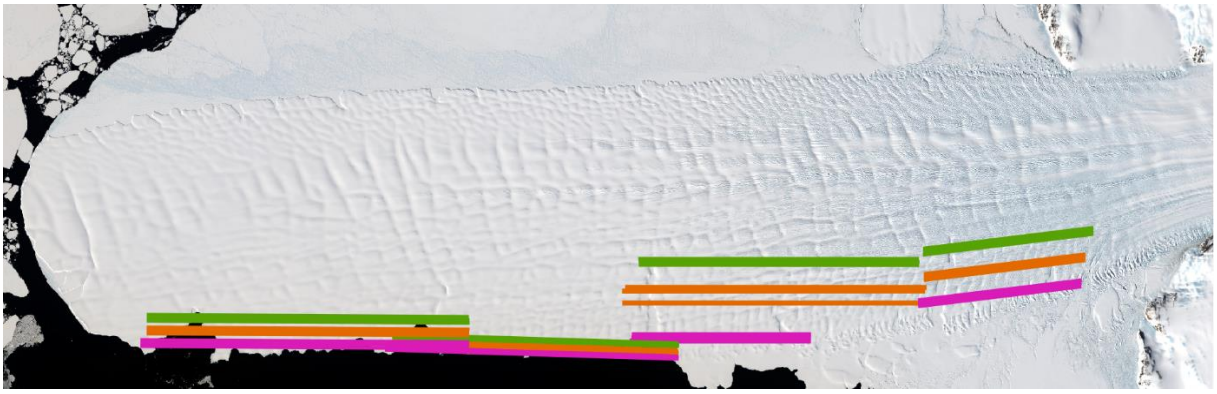

Figure 1.7. Guide lines used to measure changes in the front position and advancement of 4 large fractures along the ice tongue. Image source: natural colour (bands 4-3-2) Landsat 8 OLI/TIRS path 61 row 114, acquisition date: 30 December 2017.

Figure 1.8. Close up of guide lines used to measure velocity by tracking the F1 fracture, near the terminus. Guide lines cover the distance from the earliest fracture position to the most recent position. Image source: natural colour (bands 4-3-2) Landsat 8 OLI/TIRS path 61 row 114, acquisition date: 30 December 2017.

1.5.7. Numerical modelling

The Glacier Drainage System (GlaDS) model has been applied to a synthetic Antarctic ice stream (Dow et al., 2016) and to Recovery Ice Stream in East Antarctica (Dow et al., 2018b). In this thesis GlaDS is applied to the David Glacier Catchment. GlaDS is a 2D finite element

model allowing for the development and evolution of subglacial efficient and inefficient systems. Model parameters and their values are listed in Table 3 below.

Table 3. Model parameters.

Parameter	Symbol	Value	Units
Bedrock bump height	h_r	0.08	m
Englacial void ratio	e_v	10^{-5}	
Glen's flow constant	n	3	
Gravitational acceleration	g	9.8	m s^{-2}
Ice density	ρ_i	910	kg m^{-3}
Ice flow constant	A	2.4 x 10^{-25}	
Latent heat of fusion	L	3.34 x 10^5	J kg^{-1}
Sheet width below channel	l_c	2	m
Water density	ρ_w	1000	kg m^{-3}

The GlaDS model is fully described in Werder et al. (2013). In addition to equations 1, 2, and 3 in section 1.1.1, the model incorporates the following equations to simulate sheet flow and R-channel system development. Mass conservation of the distributed sheet flow is defined by

$$\frac{\partial h}{\partial t} + \nabla \cdot \boldsymbol{q} = m \tag{5}$$

where h is the thickness of the water sheet, t is the time, **q** is the discharge, and m is a source term of water input through surface input and basal melt. Discharge **q** is determined by

$$\mathbf{q} = -kh^{\alpha}|\nabla\phi|^{\beta-2}\nabla\phi \tag{6}$$

where k is a constant of sheet conductivity, α is the first sheet flow exponent of 5/4, β is the second sheet flow exponent of 3/2, and ϕ is the hydraulic potential given by equation 1 (Werder et al., 2013).

Mass conservation of the channels is defined by

$$\frac{\partial S}{\partial t} + \frac{\partial Q}{\partial s} = \frac{\Xi - \Pi}{\rho_w L} + m_c \tag{7}$$

where S is the channel cross-sectional area, Q is the channel discharge, s is the horizontal distance along the channel, Ξ is the rate of dissipation of potential energy, Π is the rate of change of sensible heat, L is the latent heat of fusion, and m_c is the water input from the surrounding distributed sheet (Werder et al., 2013). Channel discharge Q is defined by

$$Q = -k_c S^{\alpha_c} \left|\frac{\partial \phi}{\partial s}\right|^{\beta_c - 2} \frac{\partial \phi}{\partial s} \tag{8}$$

where k_c is a constant of channel conductivity, and α_c and β_c are the same as sheet flow with 5/4 and 3/2, respectively (Werder et al., 2013). Channel cross-sectional area development (∂S/∂t) is defined by

$$\frac{\partial S}{\partial t} = \frac{\Xi - \Pi}{\rho_i L} - v_c \tag{9}$$

where (Ξ-Π)/$\rho_i L$ is the opening rate of the channel and v_c is the closing rate of the channel (Werder et al., 2013).

The model requires inputs of bed and surface elevations, basal velocity, and basal melt rates throughout the catchment area. Additionally, the model requires a mesh of the catchment area. Bed and surface elevations are from the BedMachine dataset. Basal velocity and basal melt are both determined using ISSM. The subglacial catchment for David Glacier using BedMachine data was delineated using Antarctic Mapping Tools and TopoToolbox (Schwanghart & Scherler, 2014; Greene et al., 2017). The mesh was created using this catchment margin and has been refined along the grounding line and at several subglacial lakes of interest within the catchment (Fig. 1.9). The grounding line used in this mesh is the InSAR-derived Antarctic grounding line (Rignot et al., 2016). The average edge length of the mesh is 2801 m with a minimum edge length of 261 m in the refined areas.

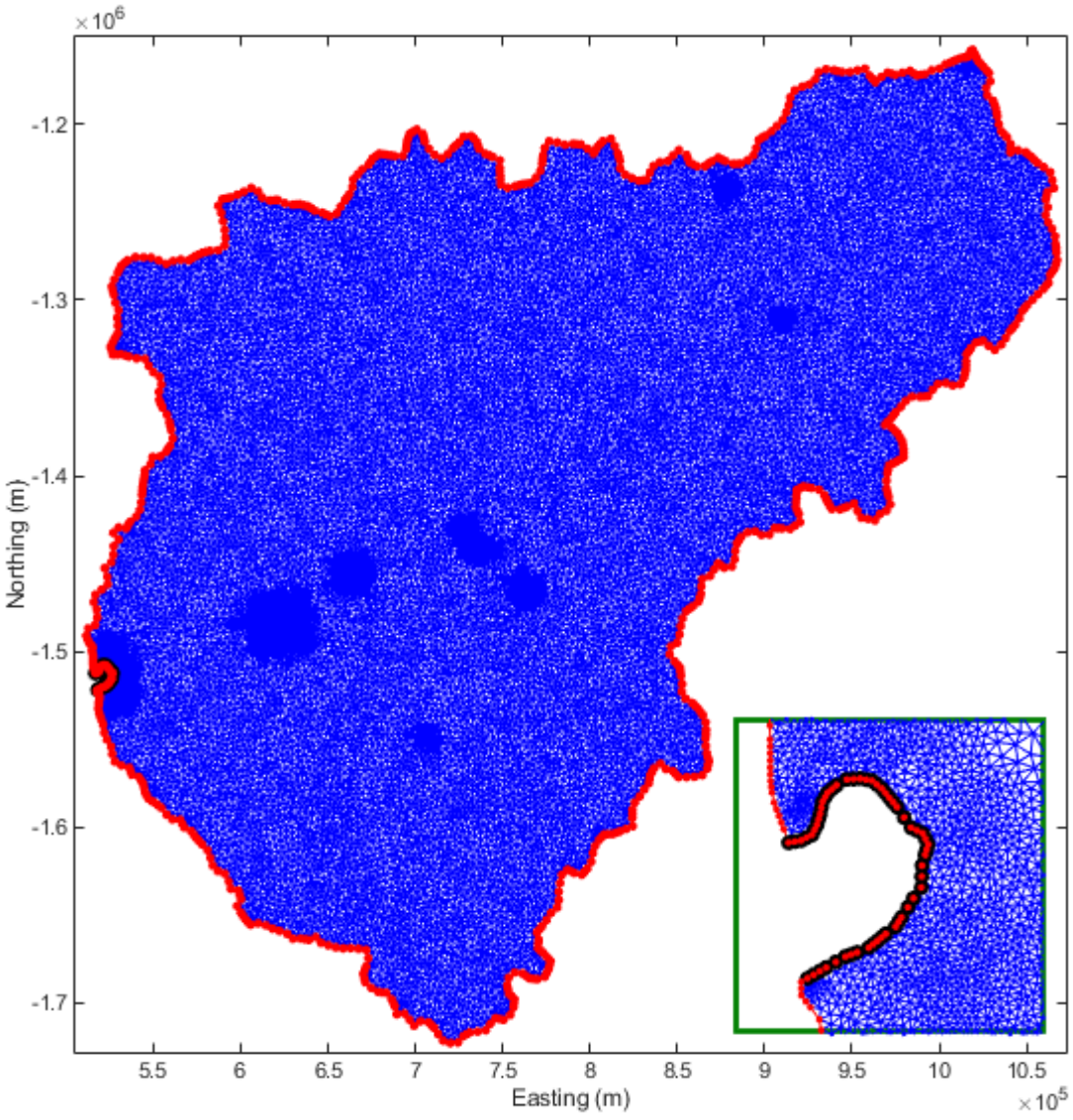

Figure 1.9. Mesh for the David Glacier catchment used in GlaDS model runs. Red circles indicate the catchment boundary. Red circles with black outlines indicate the grounding line boundary, where water is able to leave the catchment.

The model was initially run to steady state over a period of 40 years with sheet conductivity (k) of 1 x 10^{-3} $m^{7/4}$ $kg^{-1/2}$ and channel conductivity (k_c) of 5 x 10^{-2} $m^{3/2}$ $kg^{-1/2}$. Based on this initial run, sensitivity tests were run for an additional 10 years to determine the effects of sheet and channel conductivity on channel formation. Sheet conductivity values tested include 1 x 10^{-3}, 1.1 x 10^{-3}, 1 x 10^{-4}, and 1 x 10^{-5} $m^{7/4}$ $kg^{-1/2}$. Channel conductivity values tested were 5 x 10^{-1}, 5 x 10^{-2} and 5 x 10^{-3} $m^{3/2}$ $kg^{-1/2}$.

1.6. Approach to Addressing Research Objectives

The first objective of this thesis is to conduct an analysis of changes in velocity, mass loss, and fracture formation of the Drygalski Ice Tongue. I used manual feature tracking of Landsat imagery to measure annual velocity of the unconfined section of the ice front. I derived the formation dates of new fractures along the ice tongue based on ice tongue velocity and distance along the tongue for each fracture. The second objective is to simulate subglacial water movement throughout the David Catchment allowing for the identification of channelized water output at the grounding line. I applied the GlaDS model to simulate where channels form at the grounding line and compared this output with channels identified using radar ice thickness measurements. The third objective is to understand how calving events, velocity, fractures, and basal channels are related and how they influence the stability of the Drygalski Ice Tongue. I examined the propagation of five large crevasses in relation to basal channels and calving events. I tracked the formation of a new rift forming at the terminus, possibly indicating changes in stability. These three objectives are addressed in Chapter 2.

Chapter 2
Drygalski Ice Tongue stability influenced by rift formation and ice morphology

2.1. Abstract

The Drygalski Ice Tongue in East Antarctica stretches 90 km into the Ross Sea and influences local ocean circulation, access to nearby research stations, and persistence of the Terra Nova Bay polynya. To assess the stability and controls on calving of this unconfined ice tongue, we examine the propagation of five large fractures on the northern side using 21 years of Landsat imagery. We apply a subglacial hydrology model to estimate location and discharge from subglacial channels over the grounding line and compare with basal channels identified along the ice tongue using remote sensing data. Our results suggest a cyclical relationship, where large-scale calving events along marginal fractures results in the formation of new fractures closer to the grounding line. Propagation of these fractures is limited by the presence of thicker ice that persists between multiple along-ice channels that originate from water flux over the grounding line. Once the tongue thins sufficiently towards the terminus, the fractures can propagate and drive calving events. An expanding fracture at the ice tongue terminus suggests a possible impending calving event and a new rifting pattern along the ice front.

2.2. Introduction

Ice tongues and ice shelves are the seaward floating extensions of glaciers, draining interior continental ice into the ocean. While ice shelves tend to be in embayments and are therefore in contact with the coastline, ice tongues are long and narrow, extending far beyond their connections to land. This direct interaction with the ocean makes them vulnerable to warming ocean temperatures and related mass loss from basal melting and calving. As a result of their frictional contact with land, ice shelves hold back the ice that is discharged by outlet glaciers through buttressing. Reduction of this buttressing force due to mass loss through either calving or thinning, can result in increased ice flow acceleration (Rignot et al., 2004; Scambos et al., 2004; Hogg et al., 2017). It is unclear whether ice tongues have this same buttressing effect, due to their limited connection to land. Some, for example Thwaites Glacier Tongue in West Antarctica, are argued to play a minimal role in buttressing (MacGregor et al., 2012; Parizek et

al., 2013), whereas others, such as Petermann Glacier in Greenland, do provide buttressing and influence the flow of the glacier feeding the tongue (Rückamp et al., 2019). The stability of ice tongues and ice shelves is influenced by basal channels that are formed by enhanced melting at the ice-ocean interface (Rignot & Steffen, 2008; Pritchard et al., 2012; Vaughan et al., 2012; Alley et al., 2016). Some of these channels are formed from ocean melting alone whereas others are likely associated with outflow from subglacial channels over the grounding line (Le Brocq et al., 2013; Alley et al., 2016). The presence of fractures is also important for floating ice stability. Some are driven by changing stress conditions in the marginal region (Benn et al., 2007) while others are influenced by the presence of basal channels (Dow et al., 2018b; Alley et al., 2019).

Ice tongues can be found all around the coast of Antarctica, with several in East Antarctica extending into the Ross Sea. Along the Victoria Land coast alone are at least 14 ice tongues, including the Drygalski Ice Tongue, the largest in the region (SCAR Secretariat, 1992). The Drygalski Ice Tongue is ~140 km long from the grounding line, with a ~90 km unconfined floating extension into the Ross Sea. This is considerably larger than other ice tongues in the area, including Erebus Glacier Tongue and the Campbell Glacier Tongue, both less than 15 km in length (Han and Lee, 2014; Stevens et al., 2014). Wuite et al., (2009) suggested that the length of the Drygalski Ice Tongue is controlled by the occurrence of large calving events, compared to other ice tongues such as Mertz Glacier Tongue, where the calving cycle is determined by the bed topography (Wang et al., 2016).

The Drygalski Ice Tongue is fed by the David Glacier, which drains an area of ~213,500 km^2 of the interior East Antarctic Ice Sheet (Rignot et al., 2019). David Glacier is the largest glacier in the Victoria Land region (Frezzotti et al., 2000). Much of the David Glacier catchment area is below sea level, making it potentially vulnerable to ocean-driven retreat. In addition, this ice tongue plays a role in local oceanographic conditions. It holds back sea ice to the south of the ice tongue and contributes to the formation of the Terra Nova Bay polynya to the north of the ice tongue (Frezzotti & Mabin, 1994; Stevens et al., 2017), which between 2005 and 2010 ranged in size between 600 km^2 to 1000 km^2 (Ciappa et al., 2012). Velocity of the ice tongue has been found to range from a minimum of around 500 m a^{-1} at the grounding line (Rignot, 2002) to a maximum of 750-900 m a^{-1} near the terminus (Frezzotti & Mabin, 1994; Wuite et al., 2009). The Drygalski Ice Tongue has had three significant calving events since the early 1900s, with the

most recent occurring in 2005-2006 (Frezzotti & Mabin, 1994; Parmiggiani & Fragiacomo, 2005; Stevens et al., 2017). The first calving event is suggested to have occurred in the early 1900s by Holdsworth (1985) and Frezzotti & Mabin (1994). The second calving event occurred between 1956 and 1957 resulting in a loss of 40 km of the ice tongue (Frezzotti & Mabin, 1994). The most recent calving event is comprised of three separate calving events occurring between February 2005 and March 2006. Here, we refer to this recent calving as the 2005-2006 calving event. In February 2005, 74.3 km^2 of the calving front of the ice tongue calved off (Parmiggiani & Fragiacomo, 2005). In April 2005, iceberg B-15 collided with the ice tongue, breaking off an additional 64.5 km^2 leaving a narrow projecting tip (Wuite et al., 2009). On 29 March 2006, iceberg C16 collided with the tongue, breaking off the remaining portion of the tip and creating an even calving front shape (MacAyeal et al., 2008). The total surface area lost during the 2005-2006 calving events was almost 300 km^2 (Wuite et al., 2009). Between all three of these large-scale calving events is a temporal gap of ~50 years. While the Drygalski Ice Tongue has previously been stable for a long period of time, changes in its stability through calving and rift formation may indicate changing local conditions.

Analysis of the ice volumes lost during these calving events along with ice shape and average ice velocity of David Glacier and Drygalski Ice Tongue have been examined by several studies (Frezzotti & Mabin, 1994; Rignot, 2002; Wuite et al., 2009), yet it remains unclear what drives these calving events and what role fracture formation may have in influencing the stability of the Drygalski Ice Tongue. Here we build on these studies by investigating the connections between calving of the ice tongue front and the formation of new large fractures using remote sensing methods. We use 21 years of Landsat imagery to analyze the formation and evolution of several large fractures. Ice thickness is estimated using hydrostatic equilibrium calculations from surface elevation data and with airborne radar surveys over the ice tongue. We also use radar data to examine the ice draft across the width of the ice tongue to examine basal channels running along the length of the ice tongue. Finally, we apply the Glacier Drainage System (GlaDS) model to examine subglacial water flux over the grounding line from David Glacier, which is compared to the location and size of ice shelf basal channels that we identify through remote sensing and radar data. Determining the controls on the ice tongue's calving frequency and its length are necessary boundary conditions to any prognostic modeling efforts that will aim to predict future rates of ice tongue mass loss around the Antarctic Ice Sheet.

2.3. Study Area

The Drygalski Ice Tongue is located in Victoria Land, East Antarctica (75.4°S, 163.5° E) and extends into the Ross Sea. It is fed by David Glacier, which flows out through the Transantarctic Mountains, between Mount Neumayer and Hughes Bluff (Frezzotti, 1993). Northward drifting sea ice is blocked by the ice tongue, building up on its southern side. The remaining sea ice flows past the calving front, contributing to the formation of the Terra Nova Bay polynya (Bromwich & Kurtz, 1984). Ice that calves from the Ross Ice Shelf occasionally collides with the ice tongue. Four research stations are located in Terra Nova Bay around 80-90 km to the north of the ice tongue: the South Korean Jang Bogo Station, the Italian Mario Zucchelli Station, the German Gondwana Station, and a new Chinese research station on Inexpressible Island. Using longitudinal radar profiles along the ice tongue, Tabacco et al. (2000) and Bianchi et al. (2001a, 2001b) have revealed that the ice draft is heavily rippled.

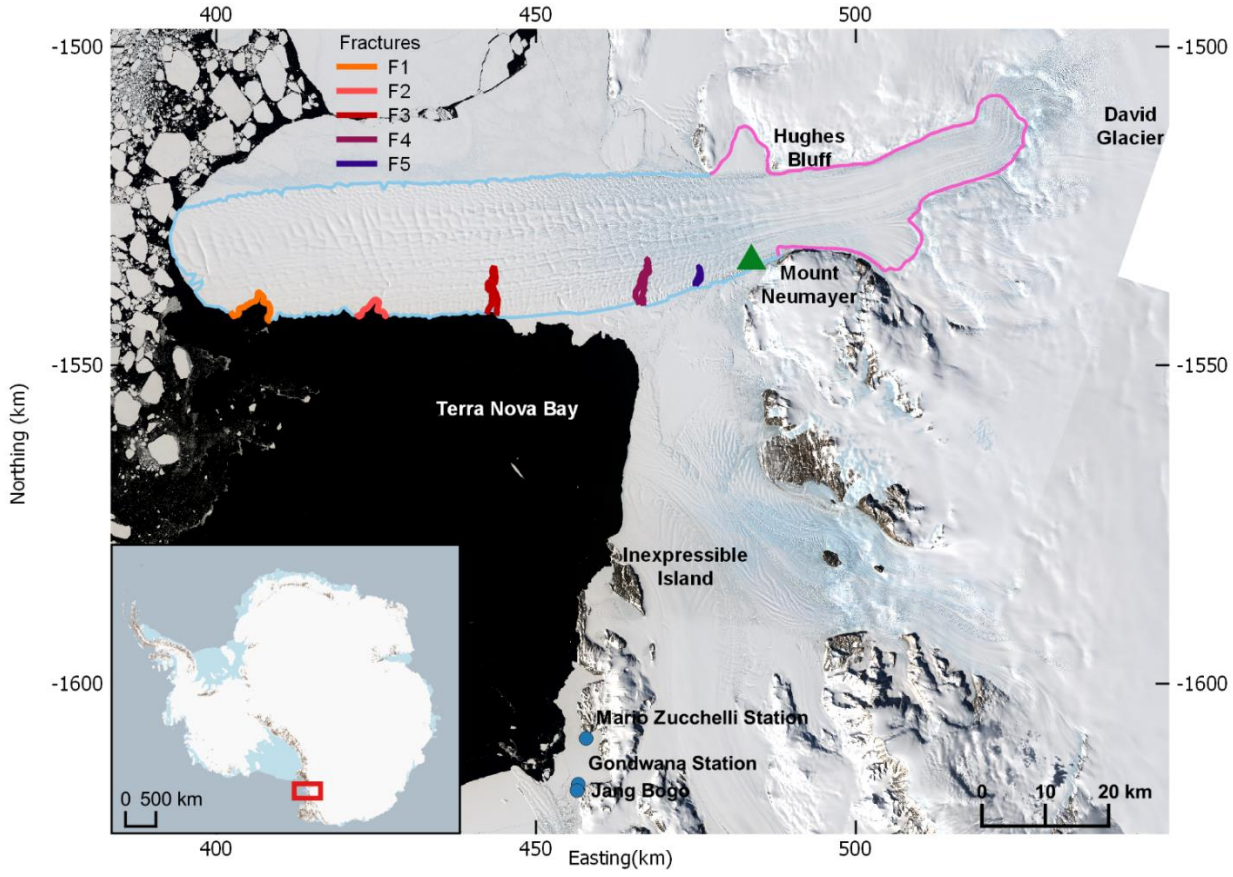

Figure 2.1. Image showing the Drygalski Ice Tongue and David Glacier: the grounding line is shown in pink, with the outline of the unconfined section of the ice tongue shown in blue. The green triangle indicates the area where fractures begin to form and is the emergence zone, where the ice tongue is no longer confined by valley walls. Inset map of Antarctica with the red box

indicates the study area. Grounding line source: MEaSUREs Antarctic Grounding Line from Differential Satellite Radar Interferometry, Version 2 (Rignot et al., 2011a, Rignot et al., 2014, Rignot et al., 2016). Image sources: Landsat 8 OLI/TIRS path 60 row 113, acquisition date: 23 December 2017; Landsat 8 OLI/TIRS path 61 row 114, acquisition date: 30 December 2017; Landsat 8 OLI/TIRS path 62 row 113, acquisition date: 6 January 2018. Inset map source: Quantarctica Database.

2.4. Methods and data sources

2.4.1. Ice tongue frontal position, fracture feature tracking, and fracture formation dates

To investigate the stability of the ice tongue, we use a combination of remote sensing imagery analysis to examine changes in the frontal position and fracture formation, and use numerical modelling of David Glacier subglacial hydrological networks to assess water flux over the grounding line and basal channel formation. Along the north side of the Drygalski Ice Tongue are five prominent fractures that persist throughout our imagery analysis period (1988 – 2018). We use imagery from Landsat 4 and 5 Thematic Mapper (TM), with 30 m resolution; Landsat 7 Enhanced Thematic Mapper Plus (ETM+) panchromatic band, with 15 m resolution; and Landsat 8 Operational Land Imager (OLI) and Thermal Infrared Sensors (TIRS) panchromatic band, with 15 m resolution. Scenes from November, December, or January were selected for each year, with total scene cloud cover below 32% (Table S1). All Landsat 7 scenes from 2003 to 2012 were affected by the SLC failure and have data gaps in the image which may interfere with feature tracking measurements where error bars cover a significant area of a fracture. Multiple images were used for years where cloud cover or data gaps obscure a fracture or the calving front in one image.

The calving front and the five prominent fractures were manually digitized from Landsat imagery for each year of available data acquired between 1988 to 2018. We used manual feature tracking techniques for each of the 5 fractures and the calving front along spatially constant guide lines. We measured the displacement of visible features along the fractures between two images separated by approximately one year. Average velocity measurements for the ice tongue were calculated from the changing position of fractures F1, F2, F3, and F4 (Fig. 2.1, Tables S4, S5, S6, S7).

The formation of F4 and F5 are identifiable in satellite imagery. Due to the limitations of available satellite data, the formation dates of F1, F2, and F3 can only be extrapolated. To

validate our extrapolation method, we also apply it to fractures F4 and F5 and verify against the satellite imagery. For the estimated formation dates of F1, F2, F3, and F4, we used the Landsat 7 image acquired on 4 January 2002 as a reference for the fracture position because this scene includes all four of these fractures. We use the average value of the fracture velocity measurements between 1989 to 2005 to represent the velocity along the unconfined section of the ice tongue. Using this 2002 Landsat image and the average velocity value of the unconfined length of the ice tongue from MEaSUREs ice velocity data (675 m a^{-1}) we can extract the approximate time interval. We derive the formation date of F5 using this same method, but with a Landsat 8 image from 24 November 2018, as the F5 fracture formed after the 2005-2006 calving event.

2.4.2. Ice draft, ice thickness, and surface elevation

We used the 8-metre resolution Reference Elevation Model of Antarctica (REMA) surface DEM to derive high-resolution ice thickness, assuming hydrostatic equilibrium (Howat et al., 2019). The surface DEM was interpolated to 25 m resolution due to file size limitations for analysis and was converted from the WGS84 ellipsoid to the GL04c geoid. Following Van den Broeke et al. (2008) we derived the actual ice thickness (*H*) from this surface DEM using

$$H = \frac{(Z_s - \Delta h)\rho_w}{\rho_w - \rho_i} + \Delta h;\ \Delta h = h_f(1 - \rho_f/\rho_i) \quad (10)$$

where Z_s is the surface elevation (metres above sea level), Δh is the firn depth correction, ρ_w is the density of seawater (1028 kg m^{-3}), and ρ_i is the density of ice (917 kg m^{-3}). The ice draft DEM was created by subtracting the ice thickness DEM from the surface DEM. We extracted across-flow transect profiles to analyse spatial change in ice draft along the ice tongue.

Firn thickness along the ice tongue is unknown, which likely introduces error in ice thickness calculations using hydrostatic equilibrium. Additionally, hydrostatically-derived ice thickness within the confined section of the tongue will be less reliable due to buttressing from the marginal bedrock. To address this, we compare the ice thickness derived from REMA with airborne ice penetrating radar and laser surface altimetry surveys that were conducted by the University of Texas Institute for Geophysics (UTIG) as part of the International Collaborative Exploration of the Cryosphere through by Airborne Profiling (ICECAP) project in October 2011.

These data provide ice thickness and surface elevation measurements for 4 transects across the width of the David Glacier and Drygalski Ice Tongue (Table S2, Fig. S5). We estimate firn thickness (h_f) for Drygalski by comparing the difference between radar-derived ice thickness and hydrostatically-derived ice thickness without firn correction. The resulting Δh values are interpolated along the ice tongue to adjust for firn in the ice thickness calculation. The Δh along the Y018a line is 0 m, while the other three lines range from 12 to 18 m. It should be noted that uncertainty in radar measurements will result in some error in the ice thickness measurement. Since we are interested in relative thickness across the ice tongue, we do not believe this will have a significant impact on our results.

2.4.3. GlaDS model setup

We applied the Glacier Drainage System (GlaDS) model to the David Glacier catchment to identify subglacial channel formation throughout the catchment and quantify channel discharge and positions at the grounding line. GlaDS is a 2D finite element model used to examine the evolution of subglacial hydrological systems, with coupled efficient and inefficient systems that co-evolve over time. GlaDS has been described in detail by Werder et al. (2013) and applied to a synthetic Antarctic ice stream in Dow et al. (2016), and to Recovery Ice Stream in East Antarctica in Dow et al. (2018b).

The catchment area draining into David Glacier was delineated in MATLAB using Antarctic Mapping Tools and TopoToolbox (Schwanghart & Scherler, 2014; Greene et al., 2017). The average edge length of the mesh is 2801 m and is refined at the grounding line giving a minimum edge length of 261 m. The grounding line used in this mesh is the InSAR-derived Antarctic grounding line (Rignot et al., 2016). Bed and surface topography DEM inputs for GlaDS are from BedMachine (Fig. S1 and S2). Bed elevations range from -1152 m to 1788 m asl and surface elevations range from 15 m to 2758 m asl within the catchment area. Values of variable basal velocity and basal melt calculated from the Ice Sheet System Model (ISSM) following a model setup similar to Seroussi et al. (2019) were used in the model runs.

We ran the model to steady state over a period of 40 years. From this, model runs were initiated with varied parameters for an additional 10 years to test the sensitivity of the model. For the David catchment, we ran several sensitivity tests with various water inputs, and sheet and

channel conductivity values. These tests were used to determine the locations of channels under various scenarios. The outputs included in this paper uses the following parameters: sheet conductivity 1 x 10^{-4} $m^{7/4}$ $kg^{-1/2}$ and channel conductivity of 5 x 10^{-1} $m^{3/2}$ $kg^{-1/2}$. This model output was selected because it had the most developed channels, extending farther upstream than the other output results. The sensitivity parameters tested include sheet conductivity of 1 x 10^{-3}, 1.1 x 10^{-3}, 1 x 10^{-4}, and 1 x 10^{-5} $m^{7/4}$ $kg^{-1/2}$. Channel conductivity values tested were 5 x 10^{-1}, 5 x 10^{-2} and 5 x 10^{-3} $m^{3/2}$ $kg^{-1/2}$.

2.5. Results

In 2018, the Drygalski Ice Tongue was 140 km long from the grounding line to the calving front, with 93 km of the ice tongue extending into the Ross Sea, unconfined by land. In 2018, the width of the ice tongue was ~13 km near the coastline, ~20 km in the middle of the ice tongue, and ~15 km at the calving front. The ice tongue is an average of 1995 m thick measured 1-2 km from the grounding line, reducing to an average of 820 m at the emergence zone and 156 m at the terminus, from our hydrostatically-derived ice thickness data. The average thickness of the entire Drygalski Ice Tongue is 720 m and is 387 m for the unconfined section. Our results are consistent with ice thickness values from BedMachine of 1740 m near the grounding line, 777 m at the emergence zone, and 228 m at the terminus.

2.5.1. Fracture formation

Two types of fractures can be identified forming along the length of the tongue: wide rifts, around 2.5 km long (F1 and F2), and narrow fractures, around 7 km long (F3, F4, and F5) (Fig. 2.1). F1, F2, F3, and F4 are spaced ~18 – 22 km apart, while F4 and F5 are spaced ~9.5 km apart. Fractures appear to form at around 75° 16.5' S, 162° 28.8' E (Fig. 2.1), where the ice tongue begins to emerge into the open ocean, near Mount Neumayer, ~50 km from the grounding line.

We estimate that F1 formed around the early 1900s, F2 in 1930, and F3 in 1959 using the method described in section 2.4.1. Fractures can be seen in the maps included in Frezzotti & Mabin (1994) but are not detailed enough to identify whether these are the same fractures. F4 formed in 1992, visible in Landsat imagery. Figure 2.2 shows an outline of F4 digitized from the

15 February 1992 Landsat 4 scene and the 14 December 1999 Landsat 7 scene. In 1992, F4 was 1.45 km in length, and by 1999 had propagated into the center of the ice tongue by 6.5 km. This equates to a propagation rate of ~645 m a^{-1}. From 1999 to 2018, the F4 fracture experienced minimal propagation with less than 500 m distance between the innermost point of the fracture from its 1999 position to its 2018 position. This is also the furthest interior extent that the F3 fracture has reached.

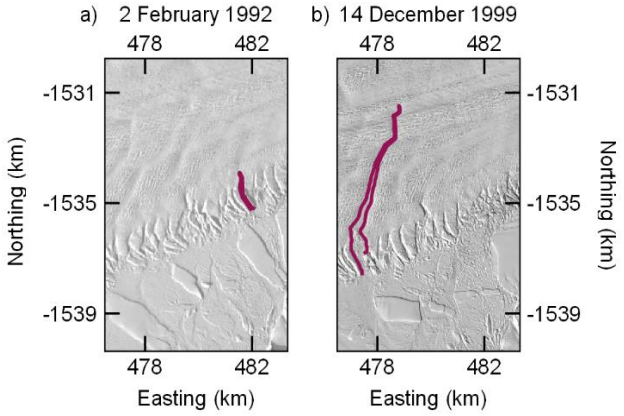

Figure 2.2. Image showing the formation and growth of the F4 fracture. Left: outline of the fracture in 1992. Right: outline of the fracture in 1999. Image source: Landsat 7 ETM+ path 63 row 113, acquisition date: 14 December 1999 (right), Landsat 4 TM path 63 row 113, acquisition date: 2 February 1992 (left).

Based on the formation date derivation method described in section 2.4.1, F5 was calculated to form in 2006, following the calving events in 2005 and 2006. In satellite imagery, the F5 fracture begins to be visible in December 2008, ~3.5 km away from the area of fracture formation (Landsat 7 20 December 2008 image). Figure S3 shows the fracture starting to become discernible from the smaller, regular fractures on 20 December 2008 with a length of 1.8 km (left image), along with the fracture development, increasing in size to a length of 2.7 km and widening to a maximum of 615 m by 20 November 2018. This equates to a propagation rate of 90 m a^{-1}. Evolution analysis of F1, F2, and F3 is not possible due to unavailability of satellite imagery for their formation periods.

Prior to the calving event in 2005-2006 the southern half of the Drygalski Ice Tongue calving front extended 14 km farther than the northern half, with a maximum width of ~14.5 km. This southern section broke off in the most recent calving event, after which the Drygalski Ice

Tongue had a more even and rectangular shape, visible in the 2006 calving front outline in Figure 2.3. Along the centre of the calving front are two small rifts incising inwards, visible in 2006 and considerably expanding by 2018. By March 2019 this rift reached a large fracture running parallel to the calving front, around 3.5 km away from the front (Fig. 2.3). This fracture is just over 2.5 km away from reaching the southern edge of the ice tongue, indicating that a calving event may occur in the near future. A calving event along this rift would result in a loss of 38 km^2 of ice.

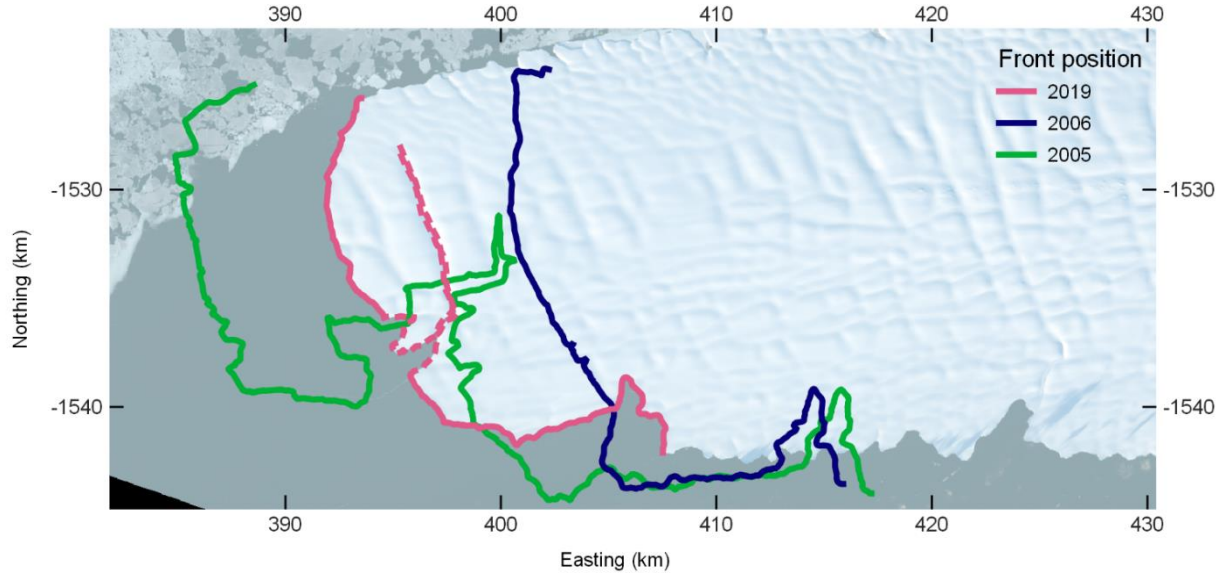

Figure 2.3. Drygalski Ice Tongue calving front outlines on 28 January 2005 (green), 17 December 2006 (dark blue), and 23 March 2019 (pink). The dashed pink line indicates the rifting section of the calving front in 2019. The 2005 outline is before the large 2005-2006 calving event, and the 2006 outline is after this event. Image source: Landsat 8 OLI/TIRS path 60 row 114, acquisition date: 24 November 2018.

2.5.2. Basal channels

REMA-derived ice draft reveals 3 large subglacial channels that persist for the length of the ice tongue and can be traced back to the grounding line. These three channels (R1, R2, R3) are also visible in the radar thickness profiles DVG/JKB2e/Y05a, DVG/JKB2e/Y10a, DVG/JKB2e/Y14a, and DVG/JKB2e/Y18a (Fig. 2.4).

The channel keels melt as the ice tongue extends further into the ocean, causing a loss of variable ice draft and related channel features for several of these potential channels. Channel R1

runs along the south section of the tongue and increases from 1.2 km to 2.4 km wide and decreases from 120 m high along to 110 m high from the Y18a profile to the Y05a profile at the terminus (Table S3). Along Y18a, R2 changes from 2.2 km wide and 245 m high and to 3.6 km wide and 135 m at the terminus. Channel R3 is 2.8 km wide and 205 m high along Y18a and 2.7 km wide and 126 m high at the terminus. As the ice tongue leaves the valley and becomes unconfined by land, around 50 km downstream from the grounding line, ice thickness sharply decreases. Thickness of the channel keels decreases between transects Y18a and Y05a likely due to a combination of spreading and melt. The ice draft is then more consistent along the unconfined length, ranging from around 178 m to 650 m thick, with an average thickness of around 388 m.

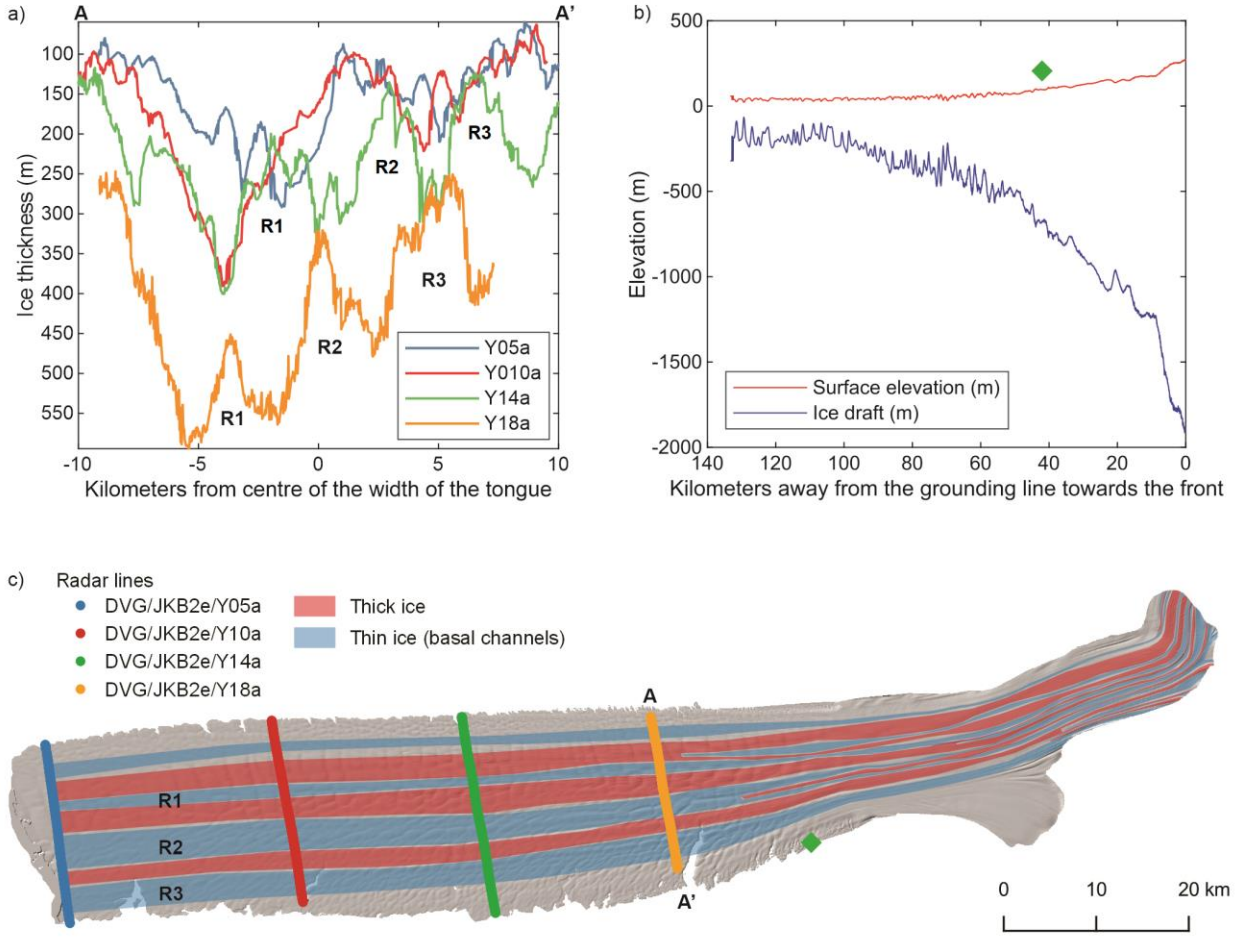

Figure 2.4. a) Radar-derived ice thickness profiles along the width of the Drygalski Ice Tongue. Transect DVG/JKB2e/Y18a is closest to the start of the ice tongue and DVG/JKB2e/Y05a is at the calving front. Individual ice thickness profiles are in Appendix A: Figure S5. b) Surface

elevation (m) and ice thickness (m) profiles along the length of the Drygalski Ice Tongue, from the grounding line (right) to the ice front (left). Data are extracted from the REMA surface DEM. c) Basal channels (thin areas of ice thickness, in blue) along the length of the David Glacier and Drygalski Ice Tongue. UTIG radar survey lines shown in Panel a are plotted above the DEM. Image source: Reference Elevation Model of Antarctica (REMA) 8-metre ice thickness (Howat et al., 2019).

GlaDS model outputs produce three channels at the grounding line (G1, G2, and G3 in Fig. 2.5). Channel G1 has the highest discharge of the three channels. G1 is located in the centre of the grounding line and is the convergence of two subglacial channels into one channel approximately 6 km upglacier of the grounding line with a smaller channel joining the main channel at the grounding line. These modelled channels initiate as far as 86 km upglacier from the grounding line. Fig. 2.5 shows channel discharge from the model output and ice thickness from REMA. These basal channels modelled in GlaDS align with basal channels that are visible in the ice thickness data. Channel G1 aligns with R1 and G2 aligns with R2, and G3 aligns with G3.

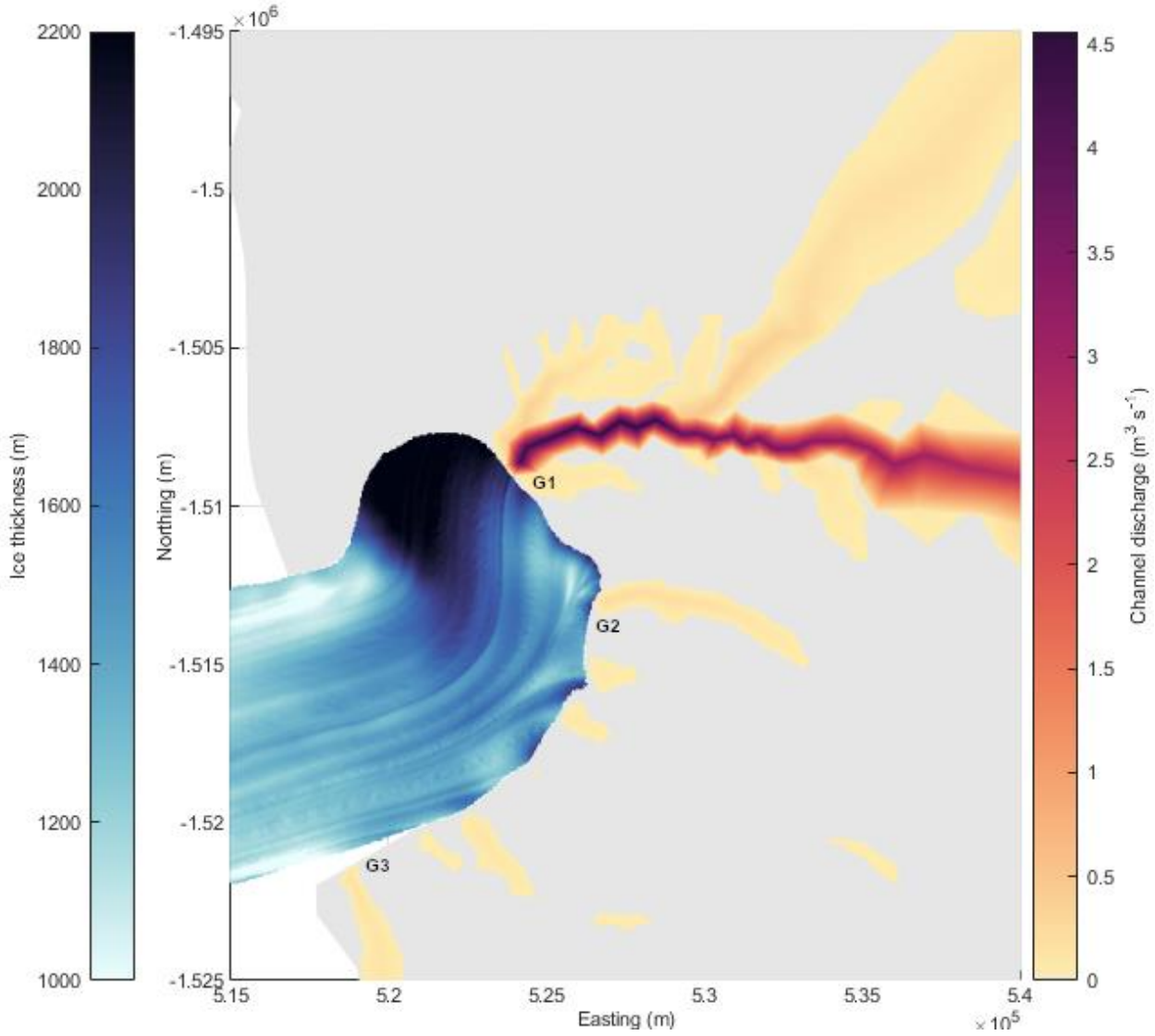

Figure 2.5. Channel discharge from GlaDS plotted with Drygalski Ice Tongue ice thickness identified using remote sensing imagery. Ice thickness (m) derived from REMA, from white (1000 m) to blue (2200), and channel discharge modelled in GlaDS, from yellow (0 m^3 s^{-1}) to purple (4.5 m^3 s^{-1})

2.6. Discussion

The Drygalski Ice Tongue can project into the Ross Sea for over 100 km past the coastline (Frezzotti & Mabin, 1994). This is considerably farther than any other ice tongue in the Victoria Land region. A recent large calving event in 2005-2006 provides an opportunity to examine the formation of a new large fracture in the ice tongue.

When we apply our extrapolation analysis to determine when the F1, F3, and F5 fractures formed, the resulting dates were around 1904, 1959 and 2006 respectively, which is comparable with the timing of the three large-scale calving events in the early 1900s, between 1956-1957, and in 2005-2006. Our results suggest that the calving events have an effect on spatial variability of longitudinal strain along the ice tongue, leading to the formation of new large fractures near the emergence zone. These rifts then create regions of weakness along the ice tongue where calving events can occur in the future. We therefore demonstrate that there is a cyclical relationship between large-scale calving and marginal fracturing that drives a future calving event. The causes of such fracturing at the emergence zone driven by calving are unclear. It is possible that the drivers of calving whether due to collision with an iceberg such as B-15 or due to storm activity, also causes increased horizontal motion of the tongue, allowing a change in the strain regime. Alternatively, the force of the frontal piece in the process of full rifting may pull the tongue towards the south with the pivot point at the emergence zone causing fracturing. Ice dynamics modeling would be required to determine the drivers of this fracturing process.

The unconfined length of the ice tongue in 2019 is 91.4 km, only ~6.6 km away from the calving front position prior to the 2005 calving event, when the ice tongue had an unconfined extent of 98 km. At 675 m a^{-1}, the average velocity of the unconfined extent from MEaSUREs ice velocity data, the ice tongue would reach its 2005 extent by 2029. However, if the ice tongue continues to calve on a 50-year cycle as suggested by prior reporting calving events (Holdsworth, 1985; Frezzotti & Mabin, 1994; Parmiggiani & Fragiacomo, 2005; Wuite et al., 2009) the next calving event would be expected to occur in the mid 2050s. At 675 m a^{-1} growth, this would add an additional 25 km to the ice tongue before then, which would be the longest recorded extent of 116 km. It is more likely that the ice tongue calves after reaching a considerable length, combined with a physical disturbance such as a violent storm which led to the 1956-1957 calving event (Frezzotti & Mabin, 1994) or another iceberg collision similar to the one that caused the most recent calving event (Wuite et al., 2009). Wuite et al. (2009) have also suggested changes in ocean-currents or wind patterns associated with the iceberg B15A as possible drivers for the 2005-2006 calving event. Alternatively, calving events may happen more frequently but have not been observed by the limited satellite data. With current velocities and extent this would suggest a 25-year calving cycle. The current expansion of a rift that is poised to break off (Fig. 2.3) suggests that calving events may be more frequent than previously implied.

The change in shape of the calving front after the most recent calving event appears to be consistent with the calving front shape described in Frezzotti & Mabin (1994). In 1960, after the calving event in 1956-1957, this tapered calving front shape had been lost, with the ice tongue calving front now exhibiting a more even, squared edge (Frezzotti & Mabin, 1994). This same change in calving front shape occurs during the 2005-2006 calving events. These events resulted in the calving front losing the large volume of mass extending on the south side, creating a more even, but more rounded shape than the calving front shape in 1960. In 2018, the calving front appeared to exhibit the start of this tapered shape again. This difference is visible in Figure S4, where the calving front and F1 outline in 2006 is overlain on the Landsat image on 24 November 2018. Additionally, the F1 fracture in 2018 doubled in size between 2006 and 2018. This would suggest that this northern corner of the calving front is the area of the tongue most susceptible to mass loss. However, two rifts along the calving front edge began propagating inwards in 2006 and in 2019 extended ~1.2 km and 1.5 km into the front of the ice tongue. The 1.5 km long rift extends along the width of the tongue, propagating southwards. As first identified by Tabacco et al. (2000), the basal draft of the ice tongue has regularly spaced ripples, which have distinct surface expressions. The 1.5 km long rift has reached the apex of one of these ripples with ice thickness of 100 m, causing the rift to continue along the ripple southwards for a further 8 km. The invasive rifting at the calving front could result in another calving event in the near future if the rift propagates far enough along the width of the tongue or if there is an external trigger. Based on the details of previous calving events and descriptions of the ice front shape, this appears to be a new rifting pattern.

The grounding line outlets of subglacial channels modelled in GlaDS line up closely with basal ice tongue channels that can be identified in the REMA ice thickness DEM and from the radar-derived ice thickness transects. Channel G1 aligns with R1, G2 aligns with R2, and G3 aligns with R3. Although G1 produces higher discharge than G2 and G3, channel R1 is smaller than R2 and R3, possibly as a result of the thicker ice along the southern half of the ice tongue. This shows a connection between the subglacial hydrology of the David catchment and the stability of the Drygalski Ice Tongue. Freshwater plumes as a result of channelized meltwater flowing out at the grounding line cause enhanced melting of the ice draft and form basal channels that are advected along the length of the ice tongue. This has been seen elsewhere with the Filchner-Ronne Ice Shelf in West Antarctica (Le Brocq et al., 2013) and with the application

of GlaDS to Getz Ice Shelf in West Antarctica (Wei et al., The Cryosphere Discussions). Further research is needed to investigate how changes in basal melt rate and channel discharge may influence the size and formation of basal channels along the ice tongue.

The basal channels along the tongue create areas of alternating thick and thin ice and interact with the observed ice marginal fractures. The fractures appear to be able to propagate inwards through the areas of thin ice of the basal channel, and stop when they reach areas of thick ice, between channels R2 and R3 (Fig. 2.4) Propagation of fractures F1, F2, and F3 is impeded by ice around 200 m thick. The thickness of the ice tongue sharply decreases where it is no longer confined by valley walls and flows into the open ocean, suggesting a strong influence from the oceanic conditions in the Ross Sea. Following this initial thinning once in the open ocean, the ice tongue thickness remains relatively constant from the coastline onwards to the ice front. Having this steady ice thickness likely contributes to the stability of the ice tongue by allowing it to persist without fractures propagating fully through the tongue. However, the entire northern half of the tongue is thinner than the southern half, which may also contribute to the weakness and deterioration of the northern corner of the calving front.

In addition to the basal channels running along the length of the ice tongue, the propagation of these large fractures appears to be influenced by the basal ripples running across the width of the ice tongue. F3 and F4 reach up to 7 km into the width of the ice tongue and are situated along the apex of two of the basal ripples while F1 and F5 are between two basal ripples, at the keel where ice is thicker and only propagate up to 3.4 km. The F2 rift is a full rift for ~2.7 km but may extend for an additional 3 km as a smaller fracture which has not penetrated through the entire thickness of the ice, as a result of connecting with one of the basal ripples. This suggests that the ability of these fractures to propagate inwards is driven by a complex ice draft morphology consisting of 3 large channels along the length of the tongue and numerous smaller ripples across the width of the tongue. This connection between fracture propagation and basal ripples may be prevalent elsewhere, such as the nearby Campbell Glacier Tongue and Aviator Glacier Tongue which also exhibit this rippled formation in the ice draft (Bianchi et al., 2001a).

The nearby Erebus Glacier Tongue (EGT) in McMurdo Sound experienced a recent calving event in 2013, which was 10 years earlier than predicted (Stevens et al., 2013). The Erebus Glacier Tongue is much smaller than the Drygalski Ice Tongue, at a length of

approximately 12.9 km long prior to calving and 9.9 km post-calving (Stevens et al., 2013). Holdsworth (1982) suggests that sea ice plays a protective role for the stability of the EGT. If the Drygalski Ice Tongue and other nearby ice tongues calve prematurely, it may indicate changing conditions in the local ocean. Further research is needed on how the presence of persistent sea ice along the Southern edge of the ice tongue may influence the stability of the Drygalski Ice Tongue. Additionally, more research is needed on the role of local oceanographic conditions on the ice tongue's stability. Modelling of ice dynamics in ISSM, or velocity mapping using automated feature tracking of high-resolution imagery would be beneficial to assess the impact of large calving events on the strain characteristics of the Drygalski Ice Tongue. The large rifts at the calving front invite continued monitoring of the Drygalski Ice Tongue and further research on the calving processes occurring here.

2.7. Conclusions

The Drygalski Ice Tongue in East Antarctica is 140 km long, with 90 km of this extending unconfined into the Ross Sea. This unconfined section is characterized by five large, regularly spaced fractures along the South side of the tongue. The ice tongue has important implications for the surrounding area, influencing the local ocean and contributing to the formation of the Terra Nova Bay polynya. The ice tongue is relatively stable, with three large calving events occurring with a period of ~50 years between, one suggested to have occurred in the early 1900s, one in 1956-1957, and in 2005-2006. We estimated the formation dates of the five fractures with the average velocity of the ice tongue and distance of each crevasse from the emergence zone. Using the Reference Elevation Model of Antarctica (REMA) surface DEM we derived ice thickness and ice draft to identify basal channels along the tongue. This is supplemented by ice thickness data collected through airborne ice penetrating radar surveys. We also applied the GlaDS model to simulate subglacial water flow throughout the catchment and to estimate the locations and discharge of several subglacial channels at the grounding line. The model output has shown three basal channels at the grounding line aligned with three basal channels visible in the ice draft. One of these channels is situated within the area of fracture formation, where fractures propagate through the thinner ice and stop once reaching the inner keel of the channel. This demonstrates the important role that floating ice bathymetry has on the stability of ice bodies and therefore suggests that changes in that bathymetry due to alterations in

ocean conditions could have important implications for future calving events of Drygalski Ice Tongue and other ice tongues and ice shelves.

Our findings suggest that the Drygalski Ice Tongue has a cyclical relationship between large calving events and large fracture formation that eventually result in additional large calving events occurring every ~50 years. This finding has implications for our understanding of interactions between fractures and floating ice stability, both for the Drygalski Ice Tongue and for other regions of the Antarctic. Two increasingly large rifts at the calving front have reached a basal ripple running across the ice tongue, where a calving event may occur earlier than the 50-year cycle, suggesting possible changes in local ocean conditions.

Chapter 3
Conclusions

3.1. Summary

The Antarctic Ice Sheet flows into ice shelves and ice tongues that float atop the ocean, fringing the Antarctic coast. The stability of Antarctica's floating ice is of increasing concern in a warming world, with the disintegration of several ice shelves occurring in the past several decades in the Antarctic Peninsula (Doake & Vaughan, 1991; Massom et al., 2018; Scambos et al., 2004). In West Antarctica, the stability of ice shelves in the Amundsen Sea Embayment have been of particular interest as this is one of the fastest-flowing regions in Antarctica and is experiencing thinning and grounding line retreat (Joughin et al., 2014; MacGregor et al., 2012; Rignot et al., 2014). In East Antarctica, over half of the length of the Mertz Glacier Tongue was lost in 2010 due to calving (Massom et al., 2015), and in Porpoise Bay several ice tongues experienced simultaneous caving events in 2007 and 2016 (Miles et al., 2017). The overall purpose of this study is to examine several factors contributing to the stability of the Drygalski Ice Tongue in East Antarctica. This ice tongue appears to be relatively stable with an extensive length of 140 km from the grounding line to terminus and with three calving events occurring at regularly spaced intervals of ~50 years. Three research objectives were outlined at the beginning of this thesis: to analyze changes in velocity, mass loss, and fracture formation of the Drygalski Ice Tongue; to model the subglacial hydrology, primarily channel formation, of the David Catchment; and to determine how calving events, velocity, fractures, and basal channels influence the Drygalski Ice Tongue's stability. Identifying how the subglacial hydrology and basal channels in the ice draft of the Drygalski Ice Tongue are related can strengthen understanding of how subglacial hydrology beneath grounded ice can impact ice shelves and ice tongues and their stability in general.

First, Landsat imagery from 1988 to 2018 was used to analyze changes in velocity, mass loss, and fracture formation. Velocity of the unconfined section of the Drygalski Ice Tongue was measured using manual feature tracking of five prominent fractures. While the average velocity of the ice tongue increased after the calving event in 2005-2006, the velocity results were too varied to support a connection between calving events and acceleration along the ice tongue (Fig. 3.1). Mass loss occurred with this 2005-2006 calving event, changing the ice front shape to an

even and more rectangular shape. Since this calving event, the ice front has continued to lose mass on the northern corner near F1 and two rifts have started propagating inwards near the centre of the ice front. In 2008, a new large fracture (F5) began to form at the emergence zone of the ice tongue. The formation dates of each of the 5 fractures were extrapolated based on their distance from the emergence zone and average velocity. Three fractures were found to coincide with the occurrence of large calving events. These crevasses likely form as a result of changes in the longitudinal stress following a calving event. A similar rift formation mechanism has been identified for several ice shelves in the Amundsen Sea Embayment, where thinning and acceleration causes marginal rifts to form (MacGregor et al., 2012).

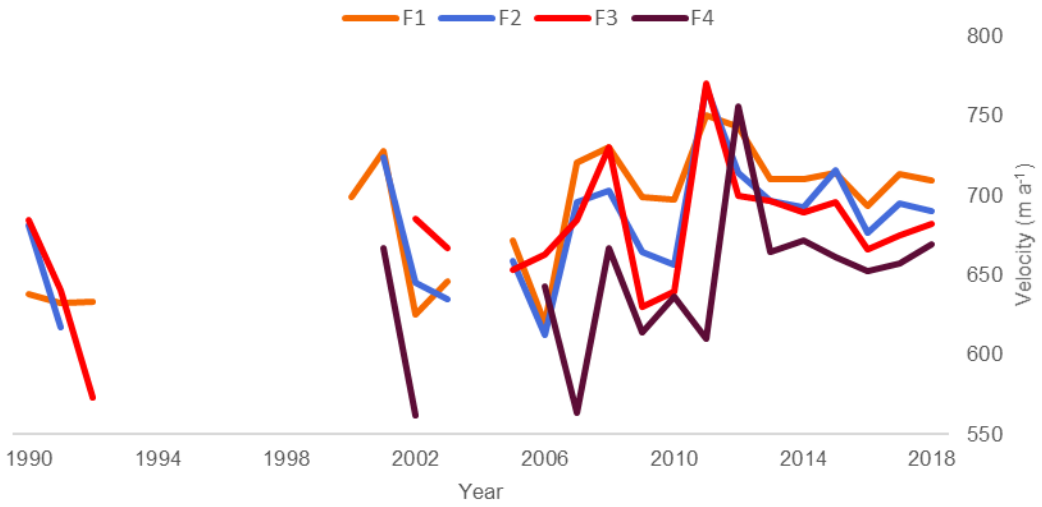

Figure 3.1 Velocity of the four fractures used in feature tracking (F1, F2, F3, F4) between 1990 and 2018.

Second, the Glacier Drainage Systems Model (GlaDS) was applied to the David Glacier catchment to simulate the movement of water beneath the ice and to identify where channelized water flows over the grounding line. The model output shows three distinct channels at the grounding line. Ice thickness transects running across the ice tongue were used to identify three basal channels along the ice draft of the ice tongue. These channels were also identified using hydrostatically-derived ice thickness based on a high-resolution surface digital elevation model. The three modelled subglacial channels align with the three channels along the ice draft

identified through ice thickness. This indicates that the location of outflow of subglacial water beneath the David Glacier controls the location of channels running along the underside of the Drygalski Ice Tongue. The basal channels in the ice draft are prominent along the length of the ice tongue, suggesting a persistent channelized system beneath the grounded ice. The buoyant freshwater discharge from subglacial channels leads to channelized melting in the ice draft as warm ocean water is entrained in these meltwater plumes, which has also been shown to occur at the Filchner-Ronne Ice Shelf (Le Brocq et al., 2013) and at several other ice shelves across Antarctica (Alley et al., 2019). This enhanced melting creates areas of thin ice and weakness, which can impact floating ice stability.

Finally, calving events, velocity, fractures, and basal channels were considered in their relation to the stability of the Drygalski Ice Tongue. While the impact of calving events on velocity changes remains unsupported, this research has identified a connection between calving events and fracture formation. After a large calving event occurs at the ice front of the Drygalski Ice Tongue, a new fracture forms at the emergence zone. The formation dates of F1, F3, and F5 (1904, 1959, and 2006) coincide with the three known calving events in the early 1900s, between 1956-1957, and in 2005-2006. This suggests a cyclical relationship in which calving events occur at the location of fractures near the terminus, causing new fractures to form which where a calving event can potentially occur. F2 is estimated to have formed in 1930 and the formation of F4 is visible in 1998. The causes of formation of these fractures is unknown, as no calving events were recorded between the early 1900s and 1956 and no large calving events occurred between the earliest Landsat image of this area in 1972 and 2005.

The length of the ice tongue from the emergence zone can be derived from maps in Frezzotti & Mabin (1994) and Wuite et al (2009). Based on the description of Douglas Mawson's map of the ice tongue in Frezzotti & Mabin (1994), in 1909 the terminus extended to a longitude of 164°42'E, equivalent to approximately 74 km from the emergence zone. Wuite et al. (2009) measure the 1956 front position to be 6.5 km from the front position in October 2000, based on a USGS map from compiled aerial photographs in Frezzotti & Mabin (1994) and RADARSAT-1 data from 2000, where the length from the emergence zone was 95 km, resulting in a length of 101.5 in 1956. The calving event in 1957 reduced the ice tongue by 40 km (Frezzotti & Mabin, 1994), resulting in a length of 61 km from the emergence zone. The change

in front position from 1909 to 1956 results in an advance rate of 703 m a^{-1} and the change from 1956 to 2005 results in an advance rate of 760 m a^{-1}. Frezzotti & Mabin (1994) report advance rates between 1909 and 1956 of 730 to 830 m a^{-1} and Wuite et al. (2009) report the advance rate from 1960 to 2000 to be 734 m a^{-1}. The 1909-1956 advance rate of 703 m a^{-1} differs from Frezzotti & Mabin (1994) due to differences in ice tongue length measurements. These results support the assumption that no calving events occurred between 1909-1956 and between 1957-2005. This suggests that F2 and F4 formed as a result of some other cause which has yet to be identified.

If the ice tongue continues to calve every 50 years, the next calving event may occur in the mid 2050s. The advancement and position of fractures can be used to predict future calving events occurring at the fracture locations. In March 2019, the F1 rift was ~7-8 km away from the position of the rift where calving occurred in 2005. At 675 m a-1, the average velocity of the unconfined extent from MEaSUREs ice velocity data, the F1 rift should advance to the 2005 position by 2029, only 23 years following the previous calving event. Using this method for the other 4 fractures, if it is assumed that calving occurs when fractures advance to a position near the large 2005 rift, then calving events based on these fractures would be: 2057 for F2 (28 year interval), 2085 for F3 (28 year interval), 2119 for F4 (34 year interval), and 2132 for F5 (13 year interval). However, calving of the ice tongue is likely to be controlled by both it's length and the influence of a physical disturbance such as violent storms (Frezzotti & Mabin, 1994) and shifting atmospheric or ocean conditions (Wuite et al., 2009).

One of the three channels in the ice draft is located along the northern side of the tongue, where the five large fractures are situated. These fractures propagate inwards through the area of thinner ice within the channel and stop propagating once they have reached the inner keel of the channel, where ice is thicker. This connection suggests that the presence and size of these basal channels plays an important role in the stability of the Drygalski Ice Tongue. If the ice tongue were to experience enhanced thinning and melting of channel keels in the future, fractures may be able to propagate further inwards, creating greater weakness in these fractured regions. Basal channels have been shown to influence fracture formation at several ice shelves in Antarctica (Dow et al., 2018a; Alley et al., 2019). Fractures along the Drygalski Ice Tongue are influenced by both basal channels along the length of the ice tongue and basal rippled across the width of

the ice tongue. While all fractures propagate into the R3 channel along the northern margin of the ice tongue, F1 and F4 are between two basal ripples and stop propagating at 3.4 km due to thicker ice at these ripple keels. F3 and F4 propagate further (7 km) as they propagate into the apex of two of the basal ripples. While the open rift of F2 propagates inwards for 2.7 km, it may extend as a smaller fracture for 3 km further into a basal ripple. These findings suggest that ice draft morphology is a key driver of fracture propagation for the Drygalski Ice Tongue and may also occur at other ice tongues and ice shelves where basal ripples and channels exist.

Rising air and ocean temperatures in a warming climate are expected to increase the amount of surface water production (Trusel et al., 2015) and basal melting (Holland et al., 2008) occurring across the Antarctic Ice Sheet and its ice shelves. Projections of Antarctica's contributions to sea level rise vary drastically, from 10 cm (Ritz et al., 2015) to 1 m (DeConto & Pollard, 2016) by 2100. Calving and basal melting are two key components to Antarctic mass balance yet remain poorly represented in models due to the complexities of these processes and the development of a universal calving law remains unsolved (Bassis, 2011). Improving the understanding of these processes is essential to model and predict how the Antarctic ice sheet and its floating ice will respond to changing atmospheric and ocean conditions. As the results of this study has shown, areas of thinner ice determine where and how far fractures can propagate in the Drygalski Ice Tongue. Enhanced basal melting due to warming ocean temperatures may result in faster fracture propagation due to increased thinning of the ice tongue.

3.2. Future work

The propagation of recent rifting at the ice front of the Drygalski Ice Tongue indicates a need for continued monitoring. This rift has reached an area of thinner ice running parallel to the ice front and may result in a calving event if the expanding fracture reaches the edge of the ice tongue. As this is a new pattern of rifting and fracture formation within the recorded history of the ice tongue, it may be an indication of changing conditions in the local ocean or other influential factors. Further research through modelling or in-situ data is needed to determine whether ocean conditions are in fact changing and what impact this may have on the future of the ice tongue's stability, or to identify what contributed to this new rift pattern.

Velocity measurements in this study were limited by the available satellite data and the use of manual feature tracking techniques. Velocity measurements in this study were based solely on Landsat imagery with a data gap between 1992 and 1999. Additionally, Landsat 7 imagery from 2003 to 2012 have data gaps due to instrument failure, limiting their usage. Remote sensing data from other satellite missions such as SPOT, ASTER, and Sentinel may be useful for filling in these gaps.

While manual feature tracking can be useful for small areas or a limited number of features, automated feature tracking can produce velocity maps along the entire length of the tongue, providing a better representation of how velocity changes from the grounding line to the terminus. Velocity maps of the Drygalski Ice Tongue and David Glacier have previously been produced prior to the most recent calving event, but it would be beneficial to create high resolution velocity maps of the ice tongue in the few years prior to and after the 2005-2006 calving event in order to identify if and where velocity changes occur. Applying an ice dynamics model may help to support the connection between calving at the ice front and fracture formation at the emergence zone.

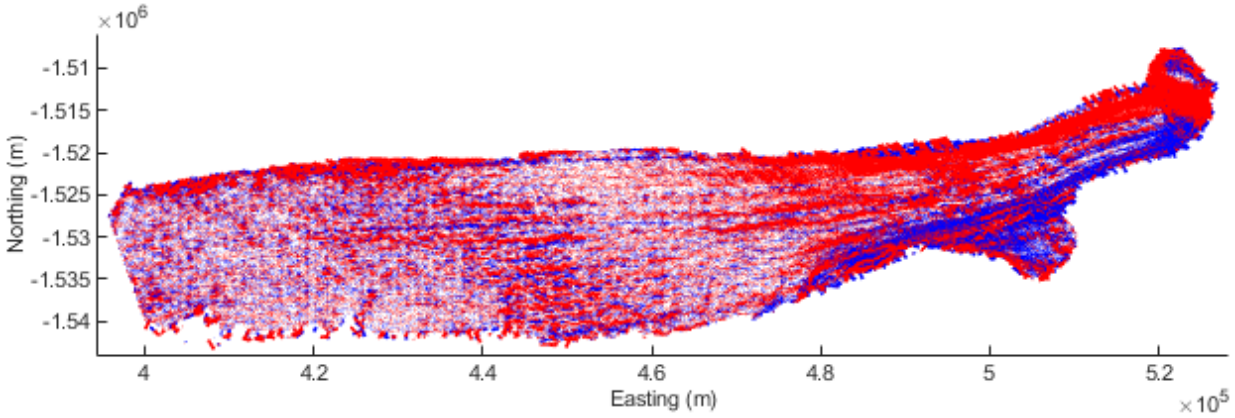

Figure 3.2. Extensional (red) and compressive (blue) strain rates along the Drygalski Ice Tongue.

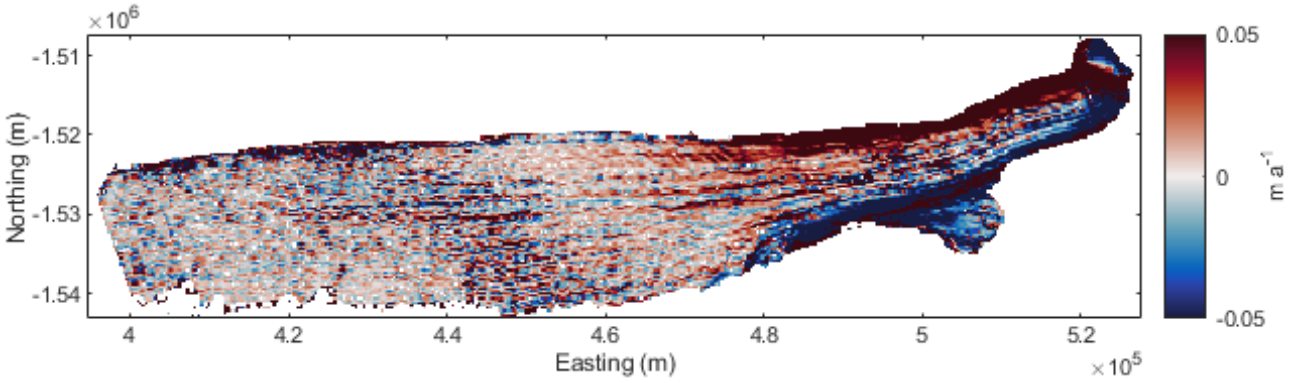

Figure 3.3. Extensional (red) and compressive (blue) strain rates along the Drygalski Ice Tongue, strain values capped between -0.05 and 0.05 m a^{-1}.

As fracture formation occurs with changes in stresses within the ice, high-resolution calculations of the surface strain-rate field along the tongue would provide insight on the formation and growth of the ice tongue's large fractures. Landsat GoLIVE imagery was used to calculate strain rates across the ice tongue to analyze the strain near the rifts and the basal channels. As GoLIVE has a spatial resolution of 600 m and a velocity error range of up to 1 m d^{-1}, the data were insufficient in representing the strain in channels. Fig. 3.2 and 3.3 show examples of the strain rate maps for the GoLIVE image L8_061_114_064_2017_300_2017_364_T2T2, where blue indicates compressional and red indicates extensional strain.

3.3. Primary findings

The primary findings of this thesis are: new marginal fractures form following large calving events of the Drygalski Ice Tongue; three subglacial channels flow over the grounding line and drive formation of basal channels in the ice draft of the ice tongue; and a cyclical relationship exists with calving creating fractures, where future calving events occur, and the propagation of these fractures are limited by thicker ice at the keel of one of these channels. These findings have larger implications for general floating ice stability, as these results show the influence that the subglacial hydrology beneath grounded ice has on floating ice. Finally, applying the connection between marginal rifting and the occurrence of large calving events can be used to predict future calving events and determine if this calving frequency is changing. The

processes and conditions influencing the stability of the Drygalski Ice Tongue may be applicable to other ice shelves and ice tongues. With rising ocean temperatures and increased basal melting expected to occur in the future, understanding the connection between fracturing processes and variable ice draft thickness is important for predicting the response of ice shelves across Antarctica to basal melting and enhanced thinning.

References

Alley, K.E., Scambos, T.A., Alley, R.B. & Holschuh, N. (2019) Troughs developed in ice-stream shear margins precondition ice shelves for ocean-driven breakup. *Science Advances*. 5 (10), 1–7.

Alley, K.E., Scambos, T.A., Siegfried, M.R. & Fricker, H.A. (2016) Impacts of warm water on Antarctic ice shelf stability through basal channel formation. *Nature Geoscience*. 9 (4), 290–293.

Bassis, J.N. (2011) The statistical physics of iceberg calving and the emergence of universal calving laws. *Journal of Glaciology*. 57 (201), 3–16.

Benn, D.I., Warren, C.R. & Mottram, R.H. (2007) Calving processes and the dynamics of calving glaciers. *Earth-Science Reviews*. 82, 143–179.

Bianchi, C., Chiappini, M., Tabacco, I.E., Passerini, A., Zirizzotti, A. & Zuccheretti, E. (2001a) Morphology of bottom surfaces of glacier ice tongues in the East Antarctic region. *Annali Di Geofisica*. 44 (1), 127–135.

Bianchi, C., Chiappini, M., Tabacco, I.E., Zirizzotti, A. & Zuccheretti, E. (2001b) Quasi-parabolic reflecting bottom surfaces of the Drygalski Antarctic floating ice tongue. *Annali Di Geofisica*. 44 (3), 619–626.

Bromwich, D.H. & Kurtz, D.D. (1984) Katabatic wind forcing of the Terra Nova Bay polynya. *Journal of Geophysical Research*. 89 (C3), 3561–3572.

Cappelletti, A., Picco, P. & Peluso, T. (2010) Upper ocean layer dynamics and response to atmospheric forcing in the Terra Nova Bay polynya, Antarctica. *Antarctic Science*. 22 (3), 319–329.

Ciappa, A., Pietranera, L. & Budillon, G. (2012) Observations of the Terra Nova Bay (Antarctica) polynya by MODIS ice surface temperature imagery from 2005 to 2010. *Remote Sensing of Environment*. 119, 158–172.

Colgan, W., Rajaram, H., Abdalati, W., McCutchan, C., Mottram, R., Moussavi, M.S. & Grigsby, S. (2016) Glacier crevasses: Observations, models, and mass balance implications. *Reviews of Geophysics*. 541, 19–161.

DeConto, R. M., & Pollard, D. (2016). Contribution of Antarctica to past and future sea-level rise. *Nature*, 531 (7596), 591–597.

Depoorter, M.A., Bamber, J.L., Griggs, J.A., Lenaerts, J.T.M., Ligtenberg, S.R.M., van den Broeke, M.R. & Moholdt, G. (2013) Calving fluxes and basal melt rates of Antarctic ice shelves. *Nature*. 502, 89–92.

Dinniman, M.S., Asay-Davis, X.S., Galton-Fenzi, B.K., Holland, P.R., Jenkins, A. & Timmermann, R. (2016) Modeling Ice Shelf/Ocean Interaction in Antarctica: A Review.

Oceanography. 29 (4), 144–153.

Doake, C.S.M. & Vaughan, D.G. (1991) Rapid disintegration of the Wordie Ice Shelf in response to atmospheric warming. *Nature*. 350 (6316), 328–330.

Dow, C.F., Werder, M.A., Nowicki, S. & Walker, R.T. (2016) Modeling Antarctic subglacial lake filling and drainage cycles. *The Cryosphere*. 10 (4), 1381–1393.

Dow, C.F., Lee, W.S., Greenbaum, J.S., Greene, C.A., Blankenship, D.D., Poinar, K., Forrest, A.L., Young, D.A. & Zappa, C.J. (2018a) Basal channels drive active surface hydrology and transverse ice shelf fracture. *Science Advances*. 4 (6), 1-9.

Dow, C.F., Werder, M.A., Babonis, G., Nowicki, S., Walker, R.T., Csatho, B. & Morlighem, M. (2018b) Dynamics of Active Subglacial Lakes in Recovery Ice Stream. *Journal of Geophysical Research: Earth Surface*. 123 (4), 837–850.

Dow, C.F., McCormack, F.S., Young, D.A., Greenbaum, J.S., Roberts, J.L. & Blankenship, D.D. (2020) Totten Glacier subglacial hydrology determined from geophysics and modeling. *Earth and Planetary Science Letters*. 531, 1–9.

Dowdeswell, J.A. & Siegert, M.J. (2003) The physiography of modern Antarctic subglacial lakes. *Global and Planetary Change*. 35 (3–4), 221–236.

Dupont, T.K. & Alley, R.B. (2005) Assessment of the importance of ice-shelf buttressing to ice-sheet flow. *Geophysical Research Letters*. 32 (4), 1–4.

Favier, L., Gagliardini, O., Durand, G. & Zwinger, T. (2012) A three-dimensional full Stokes model of the grounding line dynamics: effect of a pinning point beneath the ice shelf. *The Cryosphere*. 6 (1), 101–112.

Favier, L., Durand, G., Cornford, S.L., Gudmundsson, G.H., Gagliardini, O., Gillet-Chaulet, F., Zwinger, T., Payne, A.J. & Le Brocq, A.M. (2014) Retreat of Pine Island Glacier controlled by marine ice-sheet instability. *Nature Climate Change*. 4 (2), 117–121.

Fea, M., Minora, U., Pesaresi, C. & Smiraglia, C. (2013) Remote sensing and interdisciplinary approach for studying glaciers. *Journal of Research and Didactics in Geography*. 2 (2), 115–142.

Fountain, A.G., Glenn, B. & Scambos, T.A. (2017) The changing extent of the glaciers along the western Ross Sea, Antarctica. *Geology*. 45 (10), 927–930.

Fretwell, P., Pritchard, H.D., Vaughan, D.G., Bamber, J.L., Barrand, N.E., Bell, R., Bianchi, C., Bingham, R.G., Blankenship, D.D., Casassa, G., Catania, G., Callens, D., Conway, H., Cook, A.J., Corr, H.F.J., Damaske, D., Damm, V., Ferraccioli, F., Forsberg, R., et al. (2013) Bedmap2: Improved ice bed, surface and thickness datasets for Antarctica. *The Cryosphere*. 7 (1), 375–393.

Frezzotti, M. (1993) Glaciological study in Terra Nova Bay, Antarctica, inferred from remote sensing analysis. *Annals of Glaciology*. 1763–71.

Frezzotti, M. (1997) Ice front fluctuation, iceberg calving flux and mass balance of Victoria Land glaciers. *Antarctic Science*. 9 (1), 61–73.

Frezzotti, M. & Mabin, M.C. (1994) 20th century behaviour of Drygalski Ice Tongue, Ross Sea, Antarctica. *Annals of Glaciology*. 20, 397–400.

Frezzotti, M., Cimbelli, A. & Ferrigno, J.G. (1998) Ice-front change and iceberg behaviour along Oates and George V Coasts, Antarctica, 1912-96. *Annals of Glaciology*. 27, 643–650.

Frezzotti, M., Tabacco, I.E. & Zirizzotti, A. (2000) Ice discharge of eastern Dome C drainage area, Antarctica, determined from airborne radar survey and satellite image analysis. *Journal of Glaciology*. 46 (153), 253–264.

Fürst, J.J., Durand, G., Gillet-Chaulet, F., Tavard, L., Rankl, M., Braun, M. & Gagliardini, O. (2016) The safety band of Antarctic ice shelves. *Nature Climate Change*. 6 (5), 479–482.

Fusco, G., Budillon, G. & Spezie, G. (2009) Surface heat fluxes and thermohaline variability in the Ross Sea and in Terra Nova Bay polynya. *Continental Shelf Research*. 29 (15), 1887–1895.

Greenbaum, J. S., Blankenship, D. D., Young, D. A., Richter, T. G., Roberts, J. L., Aitken, A. R. A., … Siegert, M. J. (2015). Ocean access to a cavity beneath Totten Glacier in East Antarctica. *Nature Geoscience*, 8 (4), 294–298.

Greene, C.A., Gwyther, D.E. & Blankenship, D.D. (2017) Antarctic Mapping Tools for Matlab. *Computers & Geosciences*. 104, 151–157.

Greene, C.A., Young, D.A., Gwyther, D.E., Galton-Fenzi, B.K. & Blankenship, D.D. (2018) Seasonal dynamics of Totten Ice Shelf controlled by sea ice buttressing. *The Cryosphere*. 12 (9), 2869–2882.

Gwyther, D.E., Galton-Fenzi, B.K., Dinniman, M.S., Roberts, J.L. & Hunter, J.R. (2015) The effect of basal friction on melting and freezing in ice shelf–ocean models. *Ocean Modelling*. 95, 38–52.

Han, H. & Lee, H. (2014) Tide deflection of Campbell Glacier Tongue, Antarctica, analyzed by double-differential SAR interferometry and finite element method. *Remote Sensing of Environment*. 141, 201–213.

Hogg, A.E., Shepherd, A., Cornford, S.L., Briggs, K.H., Gourmelen, N., Graham, J.A., Joughin, I., Mouginot, J., Nagler, T., Payne, A.J., Rignot, E. & Wuite, J. (2017) Increased ice flow in Western Palmer Land linked to ocean melting. *Geophysical Research Letters*. 44 (9), 4159–4167.

Holdsworth, G. (1982) Dynamics of Erebus Glacier Tongue. *Annals of Glaciology*. 3131–137.

Holdsworth, G. (1985) 'Some effects of ocean currents and wave motion on the dynamics of floating glacier tongues', in *Antarctic Research Series*. [Online]. pp. 253–271.

Holland, P.R., Feltham, D.L. & Jenkins, A. (2007) Ice Shelf Water plume flow beneath Filchner-Ronne Ice Shelf, Antarctica. *Journal of Geophysical Research: Oceans*. 112 (5), 1–12.

Holland, P.R., Jenkins, A. & Holland, D.M. (2008) The response of Ice shelf basal melting to variations in ocean temperature. *Journal of Climate*. 21 (11), 2558–2572.

Howat, I.M., Porter, C., Smith, B.E., Noh, M.J. & Morin, P. (2019) The Reference Elevation Model of Antarctica. *The Cryosphere*. 136, 65–674.

Jacobs, S.S. (2004) Bottom water production and its links with the thermohaline circulation. *Antarctic Science*. 16 (4), 427–437.

Joughin, I., Smith, B.E. & Medley, B. (2014) Marine ice sheet collapse potentially under way for the thwaites glacier basin, West Antarctica. *Science*. 344 (6185), 735–738.

Frezzotti, M. (1993) Glaciological study in Terra Nova Bay, Antarctica, inferred from remote sensing analysis. *Annals of Glaciology*. 17, 63–71.

Le Brocq, A.M., Ross, N., Griggs, J.A., Bingham, R.G., Corr, H.F.J., Ferraccioli, F., Jenkins, A., Jordan, T.A., Payne, A.J., Rippin, D.M. & Siegert, M.J. (2013) Evidence from ice shelves for channelized meltwater flow beneath the Antarctic Ice Sheet. *Nature Geoscience*. 6 (11), 945–948.

Lenaerts, J.T.M., Van Den Broeke, M.R., Van De Berg, W.J., Van Meijgaard, E. & Kuipers Munneke, P. (2012) A new, high-resolution surface mass balance map of Antarctica (1979-2010) based on regional atmospheric climate modeling. *Geophysical Research Letters*. 39 (4), 1–5.

Liu, Y., Moore, J.C., Cheng, X., Gladstone, R.M., Bassis, J.N., Liu, H., Wen, J. & Hui, F. (2015) Ocean-driven thinning enhances iceberg calving and retreat of Antarctic ice shelves. *Proceedings of the National Academy of Sciences*. 112 (11), 3263–3268.

Lucchitta, B.K., Mullins, K.F., Allison, A.L. & Ferrigno, J.G. (1993) Antarctic glacier-tongue velocities from Landsat images: first results. *Annals of Glaciology*. 17, 356–366.

Lugli, A. & Vittuari, L. (2017) A polarimetric analysis of COSMO-SkyMed and RADARSAT-2 offset tracking derived velocities of David-Drygalski Glacier (Antarctica). *Applied Geomatics*. 9, 43–52.

MacAyeal, D.R., Bindschadler, R.A., Shabtaie, S., Stephenson, S.N. & Bentley, C.R. (1987) Force, Mass, and Energy Budgets of the Crary Ice Rise Complex, Antarctica. *Journal of Glaciology*. 33 (114), 218–230.

MacAyeal, D.R., Okal, M.H., Thom, J.E., Brunt, K.M., Kim, Y.J. & Bliss, A.K. (2008) Tabular iceberg collisions within the coastal regime. *Journal of Glaciology*. 54 (185), 371–386.

MacGregor, J.A., Catania, G.A., Markowski, M.S. & Andrews, A.G. (2012) Widespread rifting and retreat of ice-shelf margins in the eastern Amundsen Sea Embayment between 1972 and 2011. *Journal of Glaciology*. 58 (209), 458–466.

Massom, R.A., Giles, A.B., Warner, R.C., Fricker, H.A., Legrésy, B., Hyland, G., Lescarmontier, L. & Young, N. (2015) External influences on the Mertz Glacier Tongue (East Antarctica) in the decade leading up to its calving in 2010. *Journal of Geophysical Research: Earth Surface*. 120, 490–506.

Massom, R.A., Scambos, T.A., Bennetts, L.G., Reid, P., Squire, V.A. & Stammerjohn, S.E. (2018) Antarctic ice shelf disintegration triggered by sea ice loss and ocean swell. *Nature*. 558 (7710), 383–389.

Matsuoka, K., Hindmarsh, R.C.A., Moholdt, G., Bentley, M.J., Pritchard, H.D., Brown, J., Conway, H., Drews, R., Durand, G., Goldberg, D., Hattermann, T., Kingslake, J., Lenaerts, J.T.M., Martín, C., Mulvaney, R., Nicholls, K.W., Pattyn, F., Ross, N., Scambos, T., et al. (2015) Antarctic ice rises and rumples: Their properties and significance for ice-sheet dynamics and evolution. *Earth-Science Reviews*. 150, 724–745.

McGrath, D., Steffen, K., Scambos, T., Rajaram, H., Casassa, G. & Rodriguez Lagos, J.L. (2012) Basal crevasses and associated surface crevassing on the Larsen C ice shelf, Antarctica, and their role in ice-shelf instability. *Annals of Glaciology*. 53 (60), 10–18.

Mercer, J.H. (1978) West Antarctic ice sheet and CO2 greenhouse effect: a threat of disaster. *Nature*. 271 (5643), 321–325.

Meredith, M.P. & King, J.C. (2005) Rapid climate change in the ocean west of the Antarctic Peninsula during the second half of the 20th century. *Geophysical Research Letters*. 32 (19), 1–5.

Miles, B.W.J., Stokes, C.R. & Jamieson, S.S.R. (2017) Simultaneous disintegration of outlet glaciers in Porpoise Bay (Wilkes Land), East Antarctica, driven by sea ice break-up. *The Cryosphere*. 11 (1), 427–442.

Morlighem, M. (2011) *Ice sheet properties inferred by combining numerical modeling and remote sensing data*. (Doctoral dissertation).

Morlighem, M., Rignot, E., Seroussi, H., Larour, E., Ben Dhia, H. & Aubry, D. (2011) A mass conservation approach for mapping glacier ice thickness. *Geophysical Research Letters*. 38 (19), 1–6.

Morlighem, M., Rignot, E., Binder, T., Blankenship, D., Drews, R., Eagles, G., Eisen, O., Ferraccioli, F., Forsberg, R., Fretwell, P., Goel, V., Greenbaum, J.S., Gudmundsson, H., Guo, J., Helm, V., Hofstede, C., Howat, I., Humbert, A., Jokat, W., et al. (2019) Deep glacial troughs and stabilizing ridges unveiled beneath the margins of the Antarctic ice sheet. *Nature Geoscience*.

Mouginot, J., B. Scheuchl, and E. Rignot. 2012. Mapping of Ice Motion in Antarctica Using Synthetic-Aperture Radar Data, Remote Sensing. 4. 2753-2767.

Nye, J.F. (1976) Water Flow in Glaciers: Jökulhlaups, Tunnels and Veins. *Journal of Glaciology*. 17 (76), 181–207.

Parizek, B.R., Christianson, K., Anandakrishnan, S., Alley, R.B., Walker, R.T., Edwards, R.A., Wolfe, D.S., Bertini, G.T., Rinehart, S.K., Bindschadler, R.A. & Nowicki, S.M.J. (2013) Dynamic (in)stability of Thwaites Glacier, West Antarctica. *Journal of Geophysical Research: Earth Surface*. 118 (2), 638–655.

Parmiggiani, F. & Fragiacomo, C. (2005) The calving event of the Drygalski Ice Tongue of February 2005. *International Journal of Remote Sensing*. 26 (21), 4633–4638.

Pattyn, F. (2003) A new three-dimensional higher-order thermomechanical ice sheet model: Basic sensitivity, ice stream development, and ice flow across subglacial lakes. *Journal of Geophysical Research*. 108 (B8), 1-15.

Pritchard, H. D., & Vaughan, D. G. (2007). Widespread acceleration of tidewater glaciers on the Antarctic Peninsula. *Journal of Geophysical Research: Earth Surface*, 112, 1–10.

Pritchard, H.D., Ligtenberg, S.R.M., Fricker, H.A., Vaughan, D.G., van den Broeke, M.R. & Padman, L. (2012) Antarctic ice-sheet loss driven by basal melting of ice shelves. *Nature*. 484 (7395), 502–505.

Rignot, E. (2002) Mass balance of East Antarctic glaciers and ice shelves from satellite data. *Annals of Glaciology*. 34, 217–227.

Rignot, E. & Thomas, R.H. (2002) Mass Balance of Polar Ice Sheets. *Science*. 297 (5586), 1502–1506.

Rignot, E. & Steffen, K. (2008) Channelized bottom melting and stability of floating ice shelves. *Geophysical Research Letters*. 35 (2), 1–5.

Rignot, E., Casassa, G., Gogineni, P., Krabill, W., Rivera, A. & Thomas, R. (2004) Accelerated ice discharge from the Antarctic Peninsula following the collapse of Larsen B ice shelf. *Geophysical Research Letters*. 31 (18), 1–4.

Rignot, E., Mouginot, J. & Scheuchl, B. (2011a) Antarctic grounding line mapping from differential satellite radar interferometry. *Geophysical Research Letters*. 38 (10), 1–6.

Rignot, E., J. Mouginot, and B. Scheuchl. (2011b) Ice Flow of the Antarctic Ice Sheet, Science. 333. 1427-1430.

Rignot, E., Jacobs, S., Mouginot, J. & Scheuchl, B. (2013) Ice-Shelf Melting Around Antarctica. *Science*. 341 (6143), 266–270.

Rignot, E., Mouginot, J., Morlighem, M., Seroussi, H. & Scheuchl, B. (2014) Widespread, rapid grounding line retreat of Pine Island, Thwaites, Smith, and Kohler glaciers, West Antarctica, from 1992 to 2011. *Geophysical Research Letters*. 41 (10), 3502–3509.

Rignot, E., J. Mouginot, and B. Scheuchl. (2016) MEaSUREs Antarctic Grounding Line from Differential Satellite Radar Interferometry, Version 2. Boulder, Colorado USA. NASA National Snow and Ice Data Center Distributed Active Archive Center.

Rignot, E., J. Mouginot, and B. Scheuchl. (2017) MEaSUREs InSAR-Based Antarctica Ice Velocity Map, Version 2. Boulder, Colorado USA. NASA National Snow and Ice Data Center Distributed Active Archive Center.

Rignot, E., Mouginot, J., Scheuchl, B., van den Broeke, M., van Wessem, M.J. & Morlighem, M. (2019) Four decades of Antarctic Ice Sheet mass balance from 1979–2017. *Proceedings of the National Academy of Sciences*. 116 (4), 1095–1103.

Ritz, C., Edwards, T. L., Durand, G., Payne, A. J., Peyaud, V., & Hindmarsh, R. C. A. (2015).

Potential sea-level rise from Antarctic ice-sheet instability constrained by observations. *Nature*, 528, 115–118.

Röthlisberger, H. (1972) Water Pressure in Intra- and Subglacial Channels. *Journal of Glaciology*. 11 (62), 177–203.

Rott, H., Rack, W., Skvarca, P. & Angelis, H. De (2002) Northern Larsen Ice Shelf, Antarctica: further retreat after collapse. *Annals of Glaciology*. 34, 277–282.

Rückamp, M., Neckel, N., Berger, S., Humbert, A. & Helm, V. (2019) Calving Induced Speedup of Petermann Glacier. *Journal of Geophysical Research: Earth Surface*. 124 (1), 216–228.

Scambos, T.A., Hulbe, C., Fahnestock, M. & Bohlander, J. (2000) The link between climate warming and break-up of ice shelves in the Antarctic Peninsula. *Journal of Glaciology*. 46 (154), 516–530.

Scambos, T., Hulbe, C., & Fahnestock, M. (2003). Climate-Induced Ice Shelf Disintegration in the Antarctic Peninsula. *Antarctic Peninsula Climate Variability: Historical and Paleoenvironmental Perspectives*, 79, 1–14.

Scambos, T.A., Bohlander, J., Shuman, C. & Skvarca, P. (2004) Glacier acceleration and thinning after ice shelf collapse in the Larsen B embayment, Antarctica. *Geophysical Research Letters*. 31 (18), 1-4.

SCAR Secretariat (1992, updated 2015). Composite gazetteer of Antarctica. (http://gcmd.nasa.gov/records/SCAR_Gazetteer.html)

Schoof, C. (2007) Ice sheet grounding line dynamics: Steady states, stability, and hysteresis. *Journal of Geophysical Research*. 112 (F3), 1-19.

Schroeder, D. M., Blankenship, D. D., & Young, D. A. (2013). Evidence for a water system transition beneath Thwaites Glacier, West Antarctica. *Proceedings of the National Academy of Sciences*, 110 (30), 12225–12228.

Schwanghart, W. & Scherler, D. (2014) Short Communication: TopoToolbox 2 - MATLAB-based software for topographic analysis and modeling in Earth surface sciences. *Earth Surface Dynamics*. 2, 1–7.

Seroussi, H., Nowicki, S., Simon, E., Abe-Ouchi, A., Albrecht, T., Brondex, J., Cornford, S., Dumas, C., Gillet-Chaulet, F., Goelzer, H., Golledge, N.R., Gregory, J.M., Greve, R., Hoffman, M.J., Humbert, A., Huybrechts, P., Kleiner, T., Larour, E., Leguy, G., et al. (2019) initMIP-Antarctica: an ice sheet model initialization experiment of ISMIP6. *The Cryosphere*. 13 (5), 1441–1471.

Shepherd, A., Ivins, E.R., A, G., Barletta, V.R., Bentley, M.J., Bettadpur, S., Briggs, K.H., Bromwich, D.H., Forsberg, R., Galin, N., Horwath, M., Jacobs, S., Joughin, I., King, M.A., Lenaerts, J.T.M., Li, J., Ligtenberg, S.R.M., Luckman, A., Luthcke, S.B., et al. (2012) A Reconciled Estimate of Ice-Sheet Mass Balance. *Science*. 338 (6111), 1183–1189.

Shreve, R.L. (1972) Movement of Water in Glaciers. *Journal of Glaciology*. 11 (62), 205–214.

Siegert, M.J., Ross, N., Le Brocq, A.M. & Brocq, A.M. Le (2016) Recent advances in understanding Antarctic subglacial lakes and hydrology Subject Areas : Author for correspondence : *Philosophical Transactions of the Royal Society A: Mathematical, Physical and Engineering Sciences*. 374 (2059), 1-12.

Smith, B.E., Fricker, H.A., Joughin, I.R. & Tulaczyk, S. (2009) An inventory of active subglacial lakes in Antarctica detected by ICESat (2003–2008). *Journal of Glaciology*. 55 (192), 573–595.

Stevens, C.L., Sirguey, P., Leonard, G.H. & Haskell, T.G. (2013) Brief communication: 'The 2013 erebus glacier tongue calving event'. *The Cryosphere*. 7 (5), 1333–1337.

Stevens, C.L., McPhee, M.G., Forrest, A.L., Leonard, G.H., Stanton, T. & Haskell, T.G. (2014) The influence of an Antarctic glacier tongue on near-field ocean circulation and mixing. *Journal of Geophysical Research: Oceans*. 119 (4), 2344–2362.

Stevens, C., Sang Lee, W., Fusco, G., Yun, S., Grant, B., Robinson, N. & Yeon Hwang, C. (2017) The influence of the Drygalski Ice Tongue on the local ocean. *Annals of Glaciology*. 1–9.

Tabacco, I.E., Bianchi, C., Chiappini, M., Zirizzotti, A. & Zuccheretti, E. (2000) Analysis of bottom morphology of the David Glacier-Drygalski Ice Tongue, East Antarctica. *Annals of Glaciology*. 30, 47–51.

Tedesco, M. (2015) 'Remote sensing and the cryosphere', in *Remote Sensing of the Cryosphere*. 1–16.

Trusel, L.D., Frey, K.E., Das, S.B., Karnauskas, K.B., Kuipers Munneke, P., van Meijgaard, E. & van den Broeke, M.R. (2015) Divergent trajectories of Antarctic surface melt under two twenty-first-century climate scenarios. *Nature Geoscience*. 8 (12), 927–932.

U.S. Geological Survey (2016) *Landsat 8 (L8) Data Users Handbook*. Version 2.

U.S. Geological Survey (2018) *Landsat 7 (L7) Data Users Handbook*. Version 1.

Van den Broeke, M. (2008) Depth and Density of the Antarctic Firn Layer Depth and Density of the Antarctic Firn Layer. *Arctic, Antarctic, and Alpine Research*. 40 (2), 432–438.

Van den Broeke, M. (1997) Spatial and temporal variation of sublimation on Antarctica: Results of a high-resolution general circulation model. *Journal of Geophysical Research Atmospheres*. 102 (25), 29765–29777.

Van den Broeke, M., Van de Berg, W.J. & Van Meijgaard, E. (2008) Firn depth correction along the Antarctic grounding line. *Antarctic Science*. 20 (5), 513–517.

van der Veen, C.J. (2002) Calving glaciers. *Progress in Physical Geography*. 26 (1), 96–122.

Vaughan, D.G., Corr, H.F.J., Bindschadler, R.A., Dutrieux, P., Gudmundsson, G.H., Jenkins, A., Newman, T., Vornberger, P. & Wingham, D.J. (2012) Subglacial melt channels and fracture

in the floating part of Pine Island Glacier, Antarctica. *Journal of Geophysical Research: Earth Surface*. 117 (3), 1–10.

Wang, X., Holland, D.M., Cheng, X. & Gong, P. (2016) Grounding and calving cycle of Mertz Ice Tongue revealed by shallow Mertz Bank. *The Cryosphere*. 10 (5), 2043–2056.

Weertman, J. (1973) 'Can a water-filled crevasse reach the bottom surface of a glacier?', in *IASH publ*. 139–145.

Wei, W., Blankenship, D.D., Greenbaum, J.S., Gourmelen, N., Dow, C.F., Richter, T.G., Greene, C.A., Young, D.A., Lee, S., Kim, T.-W., Lee, W.S., Wåhlin, A. & Assmann, K.M. (2019) Getz Ice Shelf melt enhanced by freshwater discharge from beneath the West Antarctic Ice Sheet. *The Cryosphere Discussions*.

Werder, M.A., Hewitt, I.J., Schoof, C.G. & Flowers, G.E. (2013) Modeling channelized and distributed subglacial drainage in two dimensions. *Journal of Geophysical Research: Earth Surface*. 118 (4), 2140–2158.

Williams, M.J.M., Warner, R.C. & Budd, W.F. (2002) Sensitivity of the Amery Ice Shelf, Antarctica, to changes in the climate of the southern ocean. *Journal of Climate*. 15 (19), 2740–2757.

Wright, A. & Siegert, M. (2012) A fourth inventory of Antarctic subglacial lakes. *Antarctic Science*. 24 (06), 659–664.

Wuite, J., Jezek, K.C., Wu, X., Farness, K. & Carande, R. (2009) The velocity field and flow regime of David Glacier and Drygalski Ice Tongue, Antarctica. *Polar Geography*. 32 (3–4), 111–127.

Appendix A

Supplementary information for: Drygalski Ice Tongue stability influenced by rift formation and ice morphology

Table S1. Landsat images used in this study

Scene ID	Acquisition Date	Satellite	Sensor	Resolution
LT04_L1GS_060114_19881215_20170205_01_T2_B4	15 December 1998			
LT04_L1GS_062113_19890303_20170204_01_T2_B1	3 March 1989	Landsat 4	TM	30 m
LT04_L1GS_062113_19900117_20170131_01_T2_B3	17 January 1990			
LT04_L1GS_063113_19920215_20170124_01_T2_B1	15 February 1992			
LT05_L1GS_062113_19910128_20170127_01_T2_B3	28 January 1991	Landsat 5	TM	30 m
LE07_L1GT_060114_19991230_20170215_01_T2_B8	30 December 1999			
LE07_L1GT_059114_20000124_20170213_01_T2_B8	24 January 2000			
LE07_L1GT_061113_20010209_20170207_01_T2_B8	9 February 2001			
LE07_L1GT_061113_20011226_20170201_01_T2_B8	26 December 2001			
LE07_L1GT_060114_20020104_20170201_01_T2_B8	4 January 2002			
LE07_L1GT_062113_20021204_20170127_01_T2_B8	4 December 2002			
LE07_L1GT_061113_20030114_20170127_01_T2_B8	14 January 2003			
LE07_L1GT_060114_20050128_20170116_01_T2_B8	28 January 2005			
LE07_L1GT_060114_20061217_20170106_01_T2_B8	17 December 2006	Landsat 7	ETM+	15 m
LE07_L1GT_061114_20071211_20170101_01_T2_B8	11 December 2007			
LE07_L1GT_060114_20081120_20161224_01_T2_B8	20 November 2008			
LE07_L1GT_060114_20081206_20161224_01_T2_B8	6 December 2008			
LE07_L1GT_061114_20091216_20161218_01_T2_B8	16 December 2009			
LE07_L1GT_060114_20101212_20161211_01_T2_B8	12 December 2010			
LE07_L1GT_060114_20111113_20161205_01_T2_B8	13 November 2011			
LE07_L1GT_060114_20111215_20161204_01_T2_B8	15 December 2011			
LE07_L1GT_061114_20121208_20161128_01_T2_B8	8 December 2012			
LC08_L1GT_059114_20131103_20170428_01_T2_B8	3 November 2013			
LC08_L1GT_058114_20131214_20170427_01_T2_B8	14 December 2013			
LC08_L1GT_062113_20141229_20170415_01_T2_B8	29 December 2014			
LC08_L1GT_060114_20151218_20170331_01_T2_B8	18 December 2015			
LC08_L1GT_059114_20161127_20170317_01_T2_B8	27 November 2016	Landsat 8	OLI/ TIRS	15 m
LC08_L1GT_219130_20161214_20170316_01_T2_B8	14 December 2016			
LC08_L1GT_062113_20171119_20171205_01_T2_B8	19 November 2017			
LC08_L1GT_061114_20171230_20180103_01_T2_B8	30 December 2017			
LC08_L1GT_060114_20181124_20181124_01_RT_B8	24 November 2018			

Table S2. Ice thickness radar lines used to compare with hydrostatically derived ice thickness values

Source	PST (project-season-track)
IceBridge HiCARS 2 L2 Geolocated Ice Thickness	DVG/JKB2e/Y05a
	DVG/JKB2e/Y10a
	DVG/JKB2e/Y14a
	DVG/JKB2e/Y18a
	DVG/JKB2e/X15a
	DVG/JKB2e/X16a
	DVG/JKB2e/X17a
	DVG/JKB2e/X17b

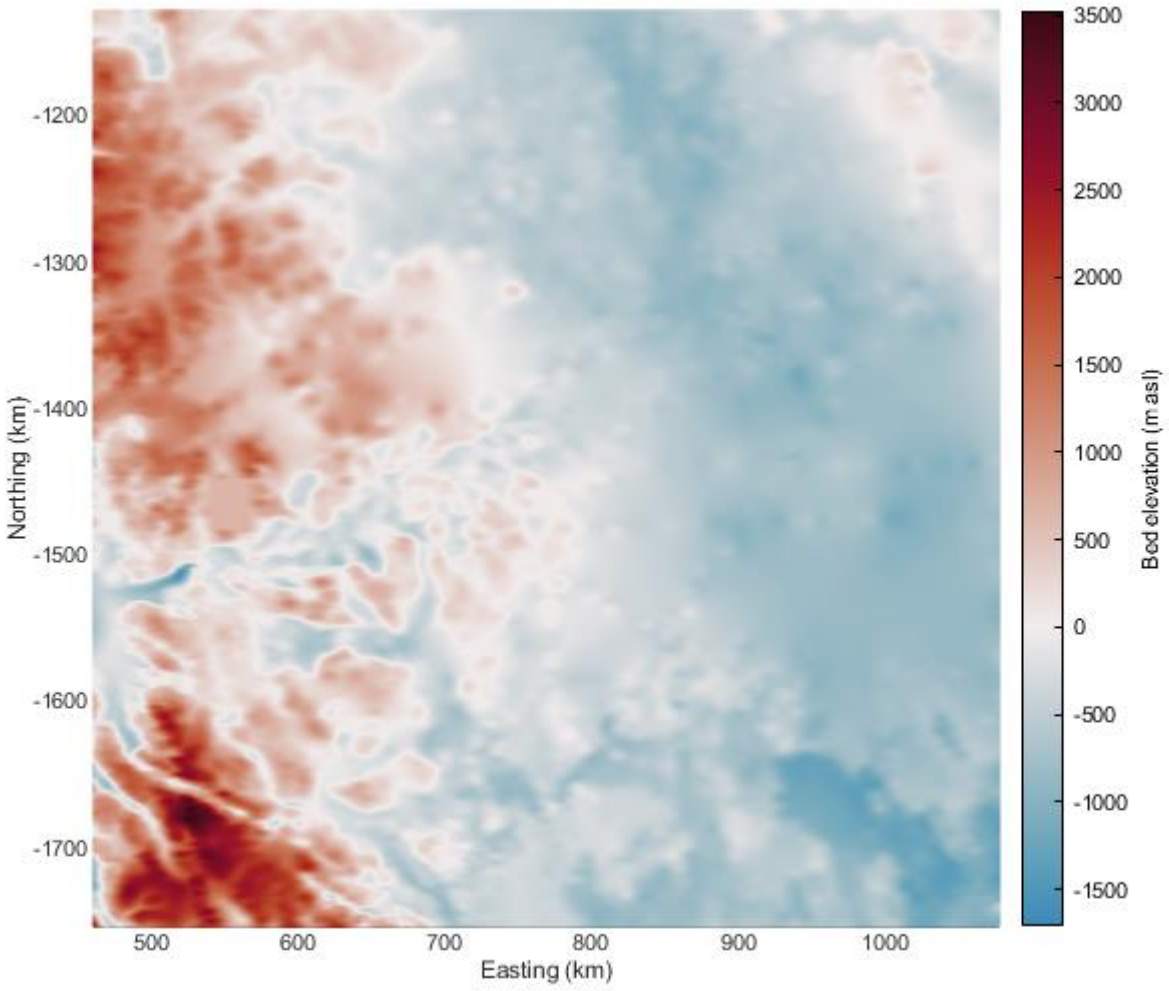

Figure S1. Bed elevation (m asl) of the David Glacier catchment from BedMachine.

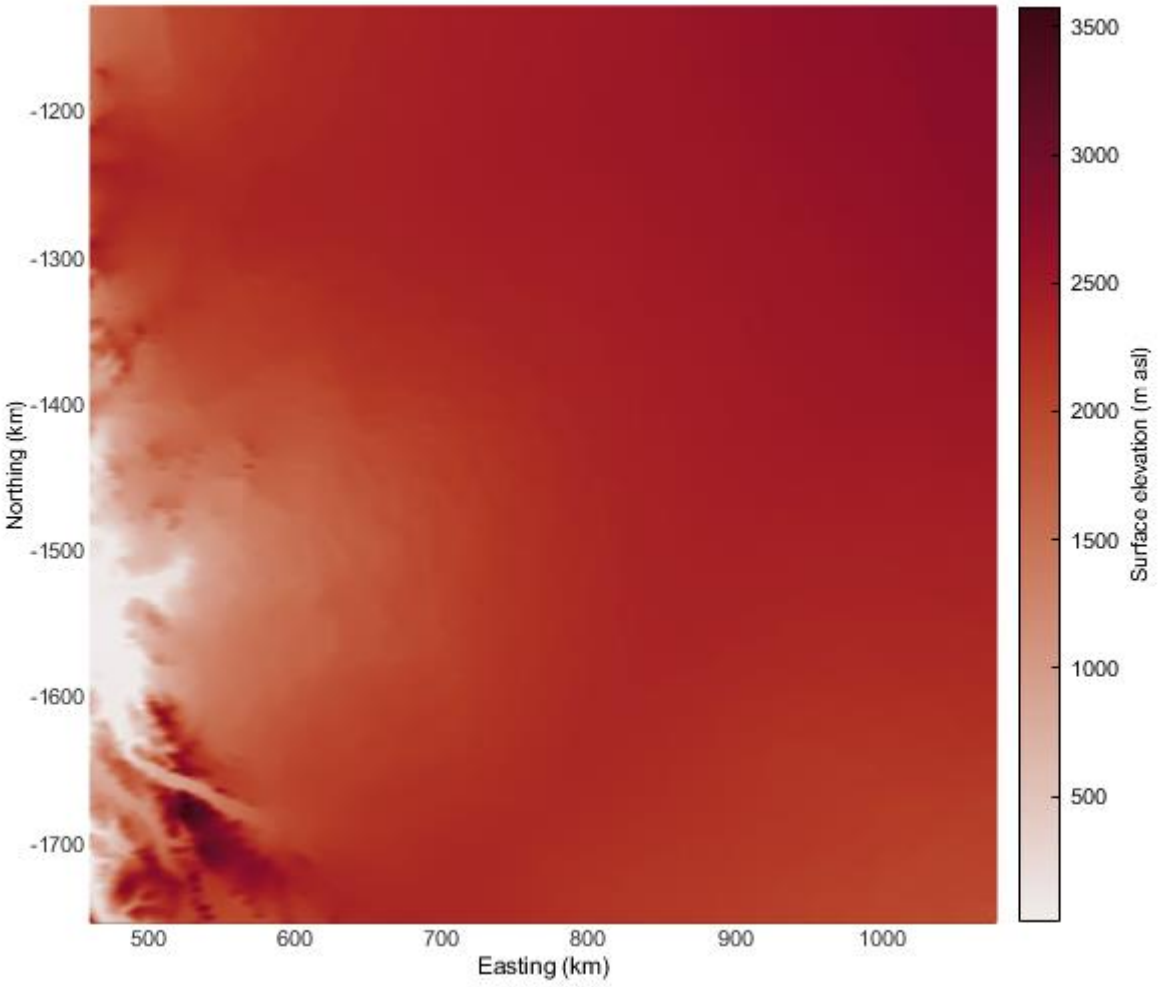

Figure S2. Surface elevation (m asl) of the David Glacier catchment from BedMachine.

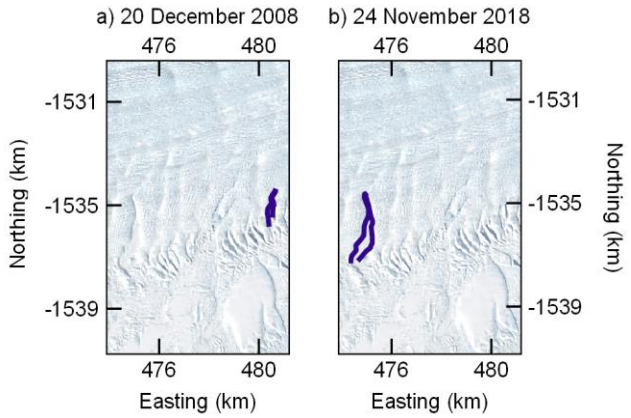

Figure S3. Image showing the formation of the F5 fracture. Left: outline of the fracture in 2008. Right: outline of the fracture in 2018. Image source: Landsat 7 ETM+ path 62 row 113, acquisition date: 20 December 2018 (left), Landsat 8 OLI/TIRS path 60 row 114, acquisition date: 24 November 2018 (right).

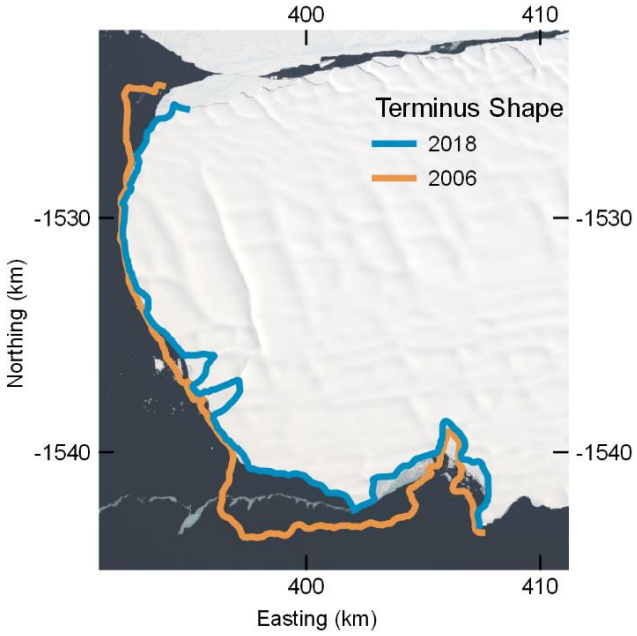

Figure S4. Comparison of the calving front shape in 2006 (orange outline) and in 2018 (blue outline). The 2006 calving front is an outline repositioned to align with the 2018 front position to compare differences in the shape and thus does not represent the actual front position. Image source: Natural colour composite (Bands 4-3-2), Landsat 8 OLI/TIRS path 60 row 114, acquisition date: 24 November 2018.

Table S3. Channel dimensions at the emergence zone (Y18a), middle of the tongue (Y14a), and terminus (Y05a) for R1, R2, and R3. Height measurements are taken from the highest point of the apex to the lowest point of the keel.

	Emergence zone height/width	Middle height/width	Terminus height/width
Channel R1	120 m / 1200 m	192 m / 3100 m	110 m / 2400 m
Channel R2	245 m / 2230 m	175 m / 2840 m	135 m / 3650 m
Channel R3	205 / 2810 m	142 m / 2520 m	126 m / 2700 m

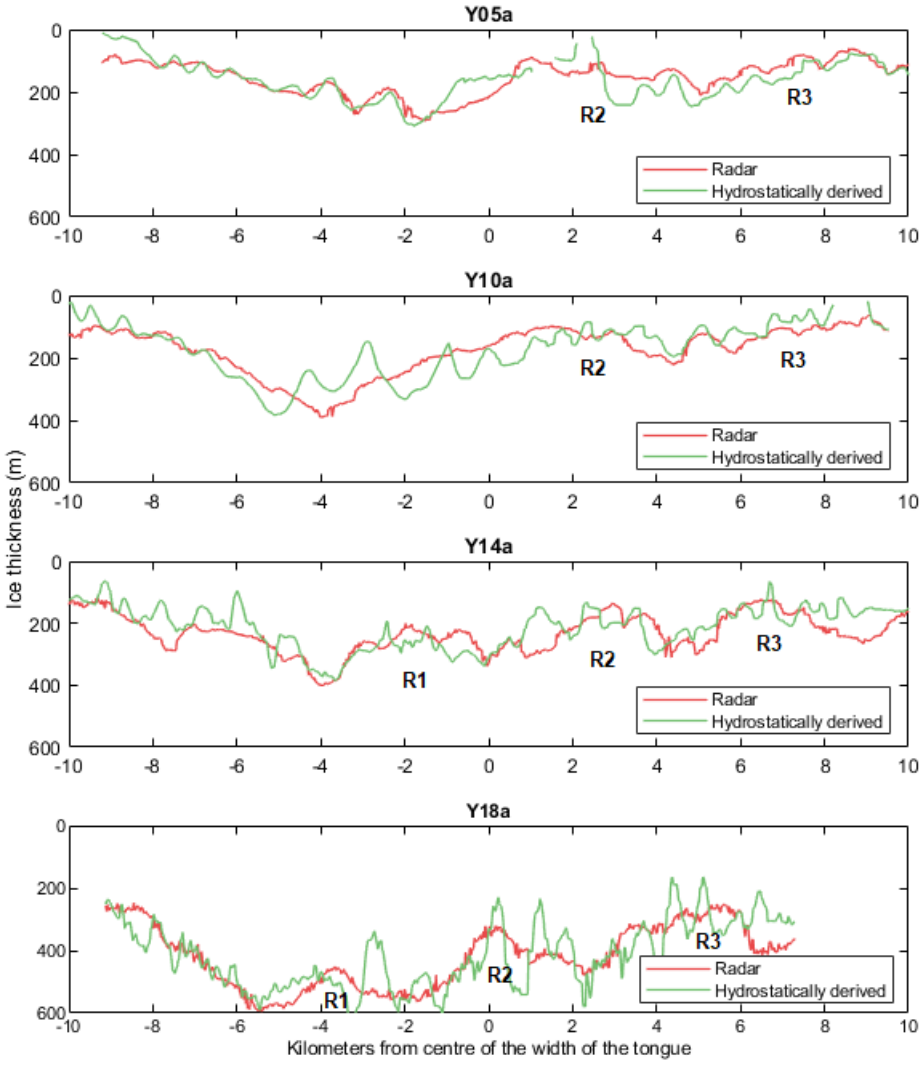

Figure S5. Individual radar ice thickness profiles for Y05a, Y10a, Y14a, and Y18a. Channels R1, R3, and R3 are indicated for each profile.

Table S4. Displacement measurements (m) between scene 1 and scene 2 and average velocity (m/year) for the F1 rift.

Scene 1	Scene 2	Average displacement between scenes (m)	Average velocity (m/year)
2017-12-30	2018-11-24	639	709
2016-12-14	2017-12-30	745	713
2015-12-18	2016-12-14	687	693
2014-12-29	2015-12-18	693	714
2013-12-14	2014-12-29	740	710
2012-12-08	2013-12-14	722	710
2011-12-15	2012-12-08	731	743
2010-12-12	2011-12-15	757	751
2009-12-16	2010-12-12	690	698
2008-12-06	2009-12-16	718	699
2007-12-11	2008-12-06	723	731
2006-12-17	2007-12-11	709	721
2005-01-28	2006-12-17	1169	620
2003-01-14	2005-01-28	1371	672
2002-01-04	2003-01-14	664	646
2001-02-09	2002-01-04	563	625
2000-01-24	2001-02-09	762	728
1992-02-15	2000-01-24	555	699
1991-01-28	1992-02-15	664	633
1990-01-17	1991-01-28	652	633
1988-12-15	1990-01-17	695	638

Table S5. Displacement measurements (m) between scene 1 and scene 2 and average velocity (m/year) for the F2 rift.

Scene 1	Scene 2	Average displacement between scenes (m)	Average velocity (m/year)
2017-12-30	2018-11-24	622	690
2016-12-14	2017-12-30	726	695
2015-12-18	2016-12-14	671	676
2014-12-29	2015-12-18	695	716
2013-12-14	2014-12-29	721	693
2012-12-08	2013-12-14	708	696
2011-11-13	2012-12-08	765	714
2010-12-12	2011-11-13	707	768
2009-12-16	2010-12-12	650	657
2008-12-06	2009-12-16	683	665
2007-12-11	2008-12-06	695	703
2006-12-17	2007-12-11	684	696
2005-01-28	2006-12-17	1154	612
2003-01-14	2005-01-28	1344	659
2002-01-04	2003-01-14	652	635
2001-02-09	2002-01-04	582	645
1999-12-30	2001-02-09	807	724
1990-01-17	1991-01-28	636	617
1989-03-03	1990-01-17	598	682

Table S6. Displacement measurements (m) between scene 1 and scene 2 and average velocity (m/year) for the F3 fracture.

Scene 1	Scene 2	Average displacement between scenes (m)	Average velocity (m/year)
2017-12-30	2018-11-24	615	682
2016-11-27	2017-12-30	736	675
2015-12-18	2016-11-27	630	667
2014-12-29	2015-12-18	675	696
2013-11-03	2014-12-29	795	689
2012-12-08	2013-11-03	630	697
2011-11-13	2012-12-08	750	700
2010-12-12	2011-11-13	710	771
2009-12-16	2010-12-12	633	640
2008-11-20	2009-12-16	675	630
2007-12-11	2008-11-20	690	730
2006-12-17	2007-12-11	674	685
2005-03-01	2006-12-17	1191	663
2003-01-14	2005-03-01	1391	654
2002-01-04	2003-01-14	685	667
2000-01-24	2002-01-04	1335	685
1992-02-15	2000-01-24	5496	692
1991-01-28	1992-02-15	602	573
1990-01-17	1991-01-28	660	641
1989-03-03	1990-01-17	600	684

Table S7. Displacement measurements (m) between scene 1 and scene 2 and average velocity (m/year) for the F4 fracture.

Scene 1	Scene 2	Average displacement between scenes (m)	Average velocity (m/year)
2017-12-30	2018-11-24	603	669
2016-11-27	2017-12-30	717	657
2015-12-18	2016-11-27	617	653
2014-12-29	2015-12-18	642	662
2012-12-08	2014-12-29	1383	672
2011-11-13	2012-12-08	712	665
2010-12-12	2011-11-13	696	756
2009-12-16	2010-12-12	603	610
2008-11-20	2009-12-16	682	637
2007-12-11	2008-11-20	580	614
2006-12-17	2007-12-11	656	667
2005-01-28	2006-12-17	1063	564
2002-12-04	2005-01-28	1384	643
2001-11-22	2002-12-04	581	562
1999-12-30	2001-11-22	1266	667